

Unveiling the origin of the capacity fade in MnO_2 zinc-ion battery cathodes through an analysis of the Mn vacancy formation

Caio Miranda Miliante,^{1,*} Kevin J. Sanders,² Liam J. McGoldrick,² Nicola Seriani,³ Brian D. Adams,⁴ Gillian R. Goward,² Drew Higgins,⁵ and Oleg Rubel¹

¹*Department of Materials Science and Engineering,
McMaster University, 1280 Main Street West,
Hamilton, Ontario L8S 4L8, Canada*

²*Department of Chemistry & Chemical Biology,
McMaster University, 1280 Main Street West,
Hamilton, Ontario L8S 4L8, Canada*

³*Condensed Matter and Statistical Physics Section,
The Abdus Salam ICTP, Strada Costiera 11, 34151 Trieste, Italy*

⁴*Salient Energy Inc., 21 McCurdy Avenue,
Dartmouth, Nova Scotia B3B 1C4, Canada*

⁵*Department of Chemical Engineering,
McMaster University, 1280 Main Street West,
Hamilton, Ontario L8S 4L8, Canada*

(Dated: February 16, 2026)

Abstract

Currently explored rechargeable aqueous zinc-ion battery (RAZIB) cathode materials, such as α -MnO₂, suffer from severe capacity fade when charging and discharging at rates appropriate for grid-scale operation. Mn dissolution has been previously identified as the cause of α -MnO₂ cathode degradation during RAZIB cycling, with conflicting evidence being found in support of the proposed Jahn-Teller effect-assisted charge disproportionation reaction as the mechanism behind Mn dissolution. In order to unveil the Mn dissolution mechanism in MnO₂ cathode cells under RAZIB operation conditions, the energetic feasibility for Mn vacancy formation was probed in both charged (MnO₂) and discharged (ZnMn₂O₄) phases of α and λ polymorphs of MnO₂ using density functional theory. The formation of a Mn vacancy, and consequently the dissolution of Mn as Mn²⁺_(aq), was found to be thermodynamically feasible for the α -ZnMn₂O₄ phase due to the energetically unfavourable Zn bent coordination formed during the Zn²⁺ intercalation process, indicating that Mn dissolution is promoted by an unstable Zn coordination environment. The theoretical calculations were then corroborated by *operando* ¹H nuclear magnetic resonance experiments which captured the Mn dissolution occurring throughout the RAZIB discharge, with subsequent electrochemical deposition of the Mn atoms on the electrode during charge. The combined computational and experimental analysis reveals the critical role of defect energetics and coordination environment in driving active material dissolution, and consequently capacity fade, with the proposed mechanism also relevant for understanding cathode degradation in other intercalating ion battery chemistries. This paper provides fundamental insight into active material dissolution mechanism, offering basis for the development of capacity fade mitigation strategies and discovery of novel cathode materials for prolonged stable battery operation.

I. INTRODUCTION

Reliable energy storage solutions are becoming essential to support the ongoing transition from fossil fuels to renewable energy [1–3]. The intermittent nature of solar and wind energy leads to an increase in demand for energy storage infrastructure, where renewable energy can be stored during surplus production and then supplied to the grid during periods of high

* miliantc@mcmaster.ca

energy demand [1, 3]. Rechargeable batteries have seen considerable increase in deployment in grid-scale energy storage due to their modular and scalable nature, being the technology behind the majority of new storage capacity gained worldwide [4–6]. Currently, lithium-ion batteries (LIBs) are the primary chemistry being utilized in rechargeable battery applications at the grid-scale, mainly due to its high energy density (up to 190 W h kg^{-1}) and cycling life (more than 1000 cycles for 80% capacity discharge) [7–9]. However, the scarcity and supply chain constraints found for LIB component manufacturing (*e.g.*, Li, Co), alongside the increase in demand for rechargeable batteries, have encouraged researchers to develop alternative battery chemistries to LIB [10–12].

One promising beyond lithium battery technology is the rechargeable aqueous zinc-ion battery (RAZIB), which is safer, has a lower associated manufacturing cost, and also has a more abundant working ion (Zn^{2+}) than LIB [5, 13, 14]. The higher safety and lower cost of manufacturing of RAZIBs can be attributed to the use of aqueous electrolytes (*e.g.*, ZnSO_4 , $\text{Zn}(\text{CF}_3\text{SO}_3)_2$, ZnCl_2), thus avoiding the flammable organic electrolytes used in LIBs which also require purpose-built dry rooms for safe battery fabrication [5, 11, 15]. RAZIBs are of special interest for implementation at the grid level because, unlike in end-consumer battery applications (*e.g.*, commercial electronics and electric vehicles), the weight and volume limits for grid-scale battery technologies are lower due to their stationary deployment [5, 13]. The commercial adoption of RAZIBs would also help to alleviate the current LIB supply constraints, as the reliance on LIBs for grid-scale energy storage applications would decrease [5, 13, 16]. However the poor cycling performance of currently investigated RAZIB cathode materials hampers the commercialization of the technology to become a reality [13].

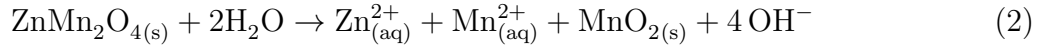
Transition metal oxides [17–24], Prussian blue analogues [25, 26], chalcogenides [27–29], and organic molecules [30–34] are some of the many materials that have already been experimentally investigated as cathode materials for RAZIB. While completely different chemical systems, one clear common aspect between all these materials is the significant capacity fade seen at practical cycling rates for grid-scale applications (more than 2 hours per cycle) [13, 29, 35–38]. Mn-based oxides stand out from all other materials as arguably the most studied cathode materials for RAZIBs. The popularity of Mn oxides can be attributed to the high operating potential (ca. 1.5 V vs Zn/Zn^{2+}), eco-friendliness, material abundance, vast number of crystal structures, low price, and wide range of Mn valency states [14, 38, 39]. The utilization of MnO_2 as a cathode in RAZIBs can be dated back to 1986, when Yamamoto

and Shoji [40] reported the cycling of the $\text{Zn}|\text{ZnSO}_4|\gamma\text{-MnO}_2$ aqueous battery system. Since then, different crystal polymorphs of MnO_2 and modifications to the oxide structure (*e.g.*, oxygen vacancy formation, ion pre-intercalation) have been investigated for improving the cycling performance of Mn oxide cathodes [13, 14, 41]. Multiple studies have previously claimed the development of highly stable MnO_2 cathode materials, achieving more than 1000 cycles with limited capacity fade when cycling at high current densities (higher than or equal to 1 A g^{-1}), consequently having discharges lasting 10 minutes or less [42–47]. While stability during fast charge/discharge cycles may be appropriate for some applications, having high stability only during fast cycling is not practical for the implementation of RAZIBs at the grid-scale, since such application requires discharge cycles lasting longer than 2 hours [5, 35].

The capacity fade seen for MnO_2 cathode materials in RAZIB has been attributed to the dissolution of the Mn atoms present in the host structure into the aqueous electrolyte as $\text{Mn}_{(\text{aq})}^{2+}$ during battery discharge [11, 17, 24, 48, 49]. The dissolved Mn atoms are then electrochemically redeposited into the electrode during the charge cycle [24, 50–52]. However, the electro-deposition of the Mn atoms occurs irregularly on the electrode surface, forming impure phases (*e.g.*, MnOOH , layered birnessite (MnO_2), ZnMn_3O_7), with the initial MnO_2 crystal structure not being completely reestablished in many cases [11, 24, 48, 50–52]. The electro-deposited Mn-containing impure phases, alongside the formation of inert phases (*e.g.*, $\lambda\text{-ZnMn}_2\text{O}_4$), would then negatively impact the capacity obtained in the following cycles, causing the capacity fade of the RAZIB [11, 17, 24, 48, 50–52]. The higher capacity loss observed during longer lasting cycling has been attributed to longer time periods spent by the electrode at low potentials, which allows for more Mn atoms to dissolve into the electrolyte as $\text{Mn}_{(\text{aq})}^{2+}$ [23]. Therefore, a thorough understanding of the Mn dissolution process, and consequently the capacity fade, during cycling rates relevant for grid-scale application is imperative to achieve the commercialization of RAZIBs. For example, by comprehending the Mn dissolution mechanism, it would then be possible to accurately identify materials that are prone to dissolution during operation and develop new strategies for capacity fade mitigation, directly guiding the design of next generation cathode materials and battery operation strategies.

The dissolution of Mn atoms as $\text{Mn}_{(\text{aq})}^{2+}$ during MnO_2 cycling has been regularly attributed to a Jahn-Teller effect (JTE)-assisted charge disproportionation reaction, where the $\text{Mn}_{(\text{s})}^{3+}$ atoms formed during battery discharge would disproportionate into $\text{Mn}_{(\text{s})}^{4+}$, which remain in

the solid phase, and soluble $\text{Mn}_{(\text{aq})}^{2+}$ species, that dissolve in the electrolyte (Eqs. (1) and (2)) [19, 48, 51, 53–57].



The JTE-assisted charge disproportionation reaction would be triggered by the formation of ZnMn_2O_4 after Zn^{2+} intercalation, with unstable JTE-active Mn^{3+}O_6 octahedra being established in the structure [19, 48, 51]. The relationship between the JTE-assisted charge disproportionation reaction and capacity fade in batteries was first proposed in the 1980s for the $\text{Li}_x\text{Mn}_2\text{O}_4$ ($1 < x < 2$) cathodes used in LIBs, with the continuous Li^+ intercalation during discharge being responsible for establishing JTE-active Mn centres [58–61]. Since then, multiple researchers have questioned the proposed JTE-assisted charge disproportionation mechanism for Mn dissolution and, consequently, the observed LIB capacity fade. For example, Berg *et al.* [62] utilized first-principle calculations to investigate the stability of fully discharged $\text{Li}_2\text{Mn}_2\text{O}_4$ cathodes and found that the JTE is crucial for stabilizing the structure, which directly contradicts the proposed mechanism of JTE-assisted charge disproportionation. Wang *et al.* [63] demonstrated through the use of rotating ring-disk experiments of a LiMn_2O_4 electrode that the concentration of $\text{Mn}_{(\text{aq})}^{2+}$ in the electrolyte would increase not only after the electrode was discharged but also after being overcharged, a phenomenon that cannot be explained by the proposed JTE-assisted charge disproportionation reaction mechanism since the charged phase is not JTE-active. Finally, Bhandari and Bhattacharya [64] presented a comprehensive review of the different proposed mechanisms for Mn dissolution in spinel cathodes during LIB cycling. The authors concluded that the JTE-assisted charge disproportionation reaction was not sufficient to explain the capacity fade observed in LIB cathodes, since Mn dissolution was demonstrated to occur even for phases that were not JTE-active [63, 65, 66].

Current RAZIB studies still directly rely on the initial proposal by LIB studies of a JTE-assisted charge disproportionation reaction mechanism to explain the Mn dissolution process occurring in Zn/MnO_2 aqueous batteries [19, 53, 56, 57]. However, key differences can be found between the operation of LIBs and RAZIBs, such as in electrolyte (non-aqueous vs aqueous), MnO_2 polymorph structure (spinel (λ) vs tunnelled (α, β, γ), layered (δ)), and

intercalating ion (Li^+ vs Zn^{2+}), which puts into question how transferable the findings from one battery chemistry can be to the other, and, to this end, whether or not the JTE-assisted charge disproportionation reaction is indeed the key mechanism behind the Mn dissolution in MnO_2 cathodes for RAZIBs.

The theoretical investigation of the formation of vacancy in solids has been successfully applied in cathodes materials for LIBs to investigate metallic dissolution and structural transformations during battery operation [67–72] and after disposal [73–76]. For example, Cai *et al.* [77] investigated the dissolution of Ni, Co, and Mn metals at different discharged states of $\text{LiNi}_x\text{Co}_y\text{Mn}_{1-x-y}\text{O}_2$ ($x \geq 0.8$) cathodes and demonstrated a direct relationship between the transition metal vacancy formation and the structural instability of the cathode material. Also, He *et al.* [78] coupled experimental results and density functional theory (DFT) calculations to study the impact of thin-film layers deposited onto the LIB cathode material on the reduction or acceleration of Mn dissolution during cycling, using vacancy formation energy calculations to probe the Mn dissolution susceptibility. Despite the significant scientific discoveries on the stability and operation of LIB cathode materials achieved through the computational investigation of vacancy formation, limited literature is available on the utilization of similar calculations to study cathode materials under RAZIB operation conditions. More importantly, to this date, the formation of Mn vacancies in MnO_2 cathodes during RAZIB operation has not been pursued, which can prove to be fundamental to uncover the key mechanism behind the Mn dissolution process, and support addressing the capacity fade experienced by the battery cells.

In this paper, a comprehensive study of the Mn dissolution process in MnO_2 cathodes under RAZIB operation condition is pursued through a first-principle investigation of the Mn vacancy formation. The Mn vacancy formation energy was calculated for both neutral and charged vacancy defects in $\alpha\text{-MnO}_2$ and $\lambda\text{-MnO}_2$ polymorphs, and their respective ZnMn_2O_4 discharged phases, capturing the thermodynamic susceptibility for Mn dissolution as $\text{Mn}_{(\text{aq})}^{2+}$ for each evaluated solid phase (*i.e.*, phase stability against Mn dissolution). Under RAZIB cycling potentials, Mn dissolution was found to be thermodynamically favourable to occur in the $\alpha\text{-ZnMn}_2\text{O}_4$ phase, which is formed through Zn^{2+} intercalation into the $\alpha\text{-MnO}_2$ cathode during discharge. The Mn dissolution mechanism was determined to be connected to a substitution reaction promoted by the unstable bent coordination for Zn in $\alpha\text{-ZnMn}_2\text{O}_4$, with a Zn atom establishing an energetically favourable octahedral coor-

dination on the vacant Mn site after Mn dissolution. The thermodynamic feasibility for Mn dissolution during RAZIB cycle of an α -MnO₂ electrode was also investigated, with Mn dissolution demonstrated to be already energetically favourable to occur for a partially discharged α -Zn_xMn₂O₄ ($x < 0.5$) phase due the unstable Zn coordination environment. Finally, *operando* ¹H nuclear magnetic resonance experiments were utilized to quantify the concentration of Mn²⁺_(aq) in the electrolyte during RAZIB cycling, with the continuous Mn dissolution from the α -MnO₂ electrode revealed to occur throughout the discharge process. After uncovering the unstable Zn coordination as the source for Mn dissolution in α -MnO₂ electrodes, potential strategies for capacity fade mitigation centred around altering the intercalating ion coordination environment were proposed, such as the inclusion of foreign atoms inside the tunnelled structure and incorporation of alloying/doping atoms in the Mn sites. The proposed dissolution mechanism can be regarded as an universally applicable degradation mechanism for battery cathodes that operate via ion intercalation, since the formation of an unstable ion coordination environment that will promote the dissolution is independent of battery chemistry. Therefore, the methodology and results presented in this study provide crucial insight into cathode material degradation, which will ultimately support addressing the battery capacity fade occurring during cycling and expedite the proposal of novel cathode materials that are stable under battery operation conditions.

II. METHODS

A. Computational Methods

Plane-wave DFT calculations with the Perdew–Burke–Ernzerhof (PBE) exchange-correlational functional [79] were carried out utilizing the Vienna *ab-initio* simulation package (VASP) [80–82] (version 6.4.3). Projector augmented wave pseudopotentials [83] for Mn, O and Zn were used, with 3p⁶4s²3d⁵, 2s²2p⁴, and 4s²3d¹⁰ valence electrons respectively considered. The plane-wave cutoff energy was set equal to the highest cutoff energy from all considered pseudopotentials, resulting in a 400 eV cutoff energy being employed. The long-range van der Waals interactions were accounted for with the use of the DFT-D3 method proposed by Grimme, with the Becke-Johnson damping function [84–88]. The Hubbard U correction for the highly correlated d electrons of Mn was considered in all calculations following the

implementation of Dudarev *et al.* [89], with the U_{eff} value equal to 3.9 eV as proposed by Jain *et al.* [90]. Spin polarization with ferromagnetic ordering was also considered for all oxides studied. Antiferromagnetic ordering was also investigated, however overall higher energy for the structures were obtained. The higher energy found for antiferromagnetic structures can be explained by the use of a high U_{eff} in our calculations, as explained by Crespo and Seriani [91]. The vacancy formation energy in $\alpha\text{-MnO}_2$ was calculated to be only of approximately 0.5 eV higher when considering antiferromagnetic ordering, a difference in magnitude which ultimately should not change the conclusions of this study.

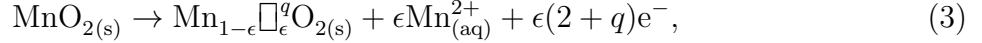
A Γ -centred k -mesh with a density of 20 subdivisions per \AA^{-1} was considered for sampling the Brillouin zone. The choice of k -mesh was verified from self-consistent (SC) calculations of the relaxed structures with a denser k -mesh, which demonstrated negligible variations in the calculated defect formation energy. Full atomic position and cell parameter relaxation was performed for all defect-free systems, with convergency tolerances of 10^{-7} eV and 10^{-2} eV \AA^{-1} respectively considered for the energy change in consecutive SC loops and for the norm of ionic forces. Only changes in the atomic positioning were allowed for the relaxation of cells containing point defects, with the same convergency tolerances being considered. A Gaussian smearing of 0.01 eV was employed in all calculations.

The $\alpha\text{-MnO}_2$ and $\lambda\text{-MnO}_2$ polymorphs were selected as representative materials for the investigation of the Mn vacancy (V_{Mn}) formation in MnO_2 cathode materials. $\alpha\text{-MnO}_2$ is a prominent and actively researched cathode material for RAZIBs. The $\alpha\text{-MnO}_2$ structure is composed of 2×2 tunnels that facilitate Zn^{2+} intercalation during battery discharge, with the structure consequently having considerably high practical capacity (greater than 200 mAh g $^{-1}$) [14, 38]. However, severe capacity fade has been reported in $\alpha\text{-MnO}_2$ cathode materials due to the dissolution of Mn atoms from the structure during battery cycling [14, 23, 38, 48, 51, 92]. On the other hand, considerably less research attention has been given to $\lambda\text{-MnO}_2$ as a cathode for RAZIBs due to the limited ion migration space in its spinel structure, which negatively impacts the possibility of Zn^{2+} intercalation [14, 93]. However, $\lambda\text{-MnO}_2$ is the only MnO_2 polymorph for which the synthesis of the Zn-containing discharged phase ZnMn_2O_4 has been experimentally confirmed [94–96]. Therefore, a more complete analysis of the impact of Zn on the formation of V_{Mn} in MnO_2 can be expected by including both the α and λ polymorphs in our study.

The unit cell structures for $\alpha\text{-MnO}_2$ (mp-19395, $2\times 2\times 3$ supercell), $\lambda\text{-MnO}_2$ (mp-25275,

$2 \times 2 \times 2$ supercell), and λ -ZnMn₂O₄ (mp-18751, $2 \times 2 \times 1$ supercell) were obtained from the Materials Project database [97], with the corresponding supercells created from the respective unit cells. The relaxed supercell lattice parameters were verified to be in agreement with the experimental unit cell lattice parameters [98–100], as shown in Table S1. It was necessary to create a supercell from each structure in order to minimize the impact of the system periodicity during the investigation of the V_{Mn} formation in the bulk materials. Unfortunately, the crystallographic structure of α -ZnMn₂O₄ has not been experimentally resolved; therefore, the α -ZnMn₂O₄ structure had to be obtained directly from first principles by incorporating Zn atoms into the α -MnO₂ tunnelled structure. The optimal Zn atom positioning inside α -MnO₂ was determined by comparing the energy from fully relaxed unit cell-sized α -ZnMn₂O₄ structures with different Zn placements investigated. The Zn placement in the lowest energy α -ZnMn₂O₄ unit cell structure was then replicated in the α -MnO₂ supercell, thus obtaining the initial α -ZnMn₂O₄ supercell structure before relaxation.

A general chemical equation for the formation of a single Mn vacancy (V_{Mn}) in MnO₂ at a charge state q with the dissolution of the Mn atom as Mn_(aq)²⁺ can be written as



where MnO_{2(s)} and Mn_{1- ϵ} \square_{ϵ}^q O_{2(s)} are the structures for MnO₂ without and with the V_{Mn}, such that $\epsilon \text{Mn}_{(\text{aq})}^{2+}$ corresponds to only 1 Mn atom. The \square_{ϵ}^q notation in Mn_{1- ϵ} \square_{ϵ}^q O_{2(s)} indicates the presence of ϵ vacancies with charge q per formula unit of the host structure. From Eq. (3), it can be seen that the formation of a V_{Mn} will be an electrochemically oxidative ($q > -2$), an electrochemically reductive ($q < -2$), or a non-electrochemical ($q = -2$) process depending on the charge q considered for the formed defect. In this article, only the formation of a neutral defect ($q = 0$) and negatively charged defect ($q = -2$) will be investigated. Investigating both defect types allows for the analysis of a scenario where the surplus charge from the V_{Mn} formation is directed to the battery system ($q = 0$) or accumulated in the cathode material ($q = -2$). An analogous chemical equation can also be established for ZnMn₂O₄:



Equations (3) and (4) outline the chemical reactions for the Mn dissolution as $\text{Mn}_{(\text{aq})}^{2+}$ through the formation of a Mn vacancy in the host structures. The energetic susceptibility for Mn dissolution from each material can then be determined through the calculation of the energy variation associated with the vacancy formation reactions (Eqs. (3) or (4)), with this parameter being known as the defect formation energy (E_d). Following the reaction paths for Eqs. (3) and (4), a negative E_d ($E_d < 0$) indicates that the Mn vacancy formation, and consequently the Mn dissolution, will be energetically favourable to occur. Conversely, a positive E_d ($E_d > 0$) will point to the Mn vacancy formation being unfeasible to occur, with the Mn atom being predicted to remain in the electrode. Apart from determining if the Mn dissolution is energetically possible, E_d will also capture the degree of instability for the phase, with a more negative E_d indicating a greater drive for the Mn dissolution reaction (*i.e.*, higher material instability).

The E_d for a single V_{Mn} in a charge state q (V_{Mn}^q) can then be calculated by [101–104]

$$E_d(\text{V}_{\text{Mn}}^q, \Delta E_F, \phi_{\text{SHE}}) = E_{\text{tot}}(\zeta(\text{V}_{\text{Mn}}^q)) - E_{\text{tot}}(\zeta(\text{host})) + \mu(\text{Mn}_{(\text{aq})}^{2+}) + q\{E_{\text{VBE}}(\zeta(\text{host})) + \Delta E_F\} + E_{\text{corr}} - (2 + q)\phi_{\text{SHE}}, \quad (5)$$

where $E_{\text{tot}}(\zeta)$ is the DFT total energy for the system ζ , $\zeta(\text{V}_{\text{Mn}}^q)$ refers to the system containing the vacancy, $\zeta(\text{host})$ is the system where the defect is being formed (*i.e.*, pristine material), $\mu(\text{Mn}_{(\text{aq})}^{2+})$ is the chemical potential of $\text{Mn}_{(\text{aq})}^{2+}$ in the condition of interest, $E_{\text{VBE}}(\zeta(\text{host}))$ is the valence band edge (VBE) energy obtained from the calculation of the host system, ΔE_F accounts for the position of the V_{Mn}^q system Fermi energy with respect to the $E_{\text{VBE}}(\zeta(\text{host}))$, E_{corr} is the energy correction term for charged defect calculations, and ϕ_{SHE} is the electrode potential vs the standard hydrogen electrode (SHE). The applied corrections were: (i) a potential alignment between the charged system and the neutral host [105], and (ii) the Freysoldt-Neugebauer-Van de Walle (FNV) correction for the spurious interactions between charged defects in finite-sized supercells [106]. The correction scheme proposed by Freysoldt *et al.* [106] allowed our energy correction to account for the anisotropy of the dielectric constant for the charged systems, which were calculated through density functional perturbation theory. The FNV correction was applied for the charged vacancy results in $\alpha\text{-MnO}_2$ and $\lambda\text{-MnO}_2$, since only for these two structures was the charged defects determined to be localized.

The chemical potential $\mu(\text{Mn}_{(\text{aq})}^{2+})$ can be calculated from

$$\mu(\text{Mn}_{(\text{aq})}^{2+}) = \mu^\circ(\text{Mn}) + \Delta\mu(\text{Mn}_{(\text{aq})}^{2+}), \quad (6)$$

where $\mu^\circ(\text{Mn})$ is the standard chemical potential of Mn, and $\Delta\mu(\text{Mn}_{(\text{aq})}^{2+})$ is the variation in the chemical potential of Mn between the standard thermodynamic condition and the condition of interest. $\mu^\circ(\text{Mn})$ can be approximated to the DFT calculated total energy per atom of Mn in its most stable polymorph ($E_{\text{tot}}(\text{Mn}_{(\text{s})}^0)$), since Mn is solid at standard conditions [101]. The tetragonal ferrimagnetic structure of α -Mn was considered here for the calculation of $E_{\text{tot}}(\text{Mn}_{(\text{s})}^0)$ following the theoretical results obtained by Hobbs *et al.* [107] on the investigation of magnetism in α -Mn. Different magnetic orderings were investigated, with the ferrimagnetic system ($0.45 \mu_B \text{ f.u.}^{-1}$) achieving the lowest total energy. The condition of interest for Mn is $\text{Mn}_{(\text{aq})}^{2+}$ ions at the concentration found for RAZIB electrolytes, given that the dissolution of Mn atoms from the cathode material into the electrolyte is being investigated. Thus, $\Delta\mu(\text{Mn}_{(\text{aq})}^{2+})$ can be calculated by

$$\Delta\mu(\text{Mn}_{(\text{aq})}^{2+}) = \Delta G^\circ(\text{Mn}_{(\text{aq})}^{2+}) + RT\ln([\text{Mn}_{(\text{aq})}^{2+}]), \quad (7)$$

where $\Delta G^\circ(\text{Mn}_{(\text{aq})}^{2+})$ is the standard Gibbs energy of $\text{Mn}_{(\text{aq})}^{2+}$ (-2.36 eV [108]), R is the ideal gas constant ($8.617 \cdot 10^{-5} \text{ eV K}^{-1} \text{ atom}^{-1}$), T is the temperature at the condition of interest (298 K), and $[\text{Mn}_{(\text{aq})}^{2+}]$ is the concentration of $\text{Mn}_{(\text{aq})}^{2+}$ in the RAZIB electrolyte. Previous studies have reported improvements in the cycling capacity and capacity retention for battery cells with MnO_2 cathodes through the addition of $\text{Mn}_{(\text{aq})}^{2+}$ into the electrolyte at concentrations around 0.1 M [109, 110]. Following the adoption by researchers of $\text{Mn}_{(\text{aq})}^{2+}$ electrolyte additives on the development of Mn-based RAZIB cathodes, a concentration of $\text{Mn}_{(\text{aq})}^{2+}$ in the electrolyte equal to 0.1 M was considered in our calculations.

The RAZIB cathode operation potential is commonly reported with respect to the Zn stripping/plating reaction occurring on the battery anode (Zn/Zn^{2+} redox couple). Therefore, the electrode potential vs Zn/Zn^{2+} (ϕ_{Zn}) can be calculated from ϕ_{SHE} by

$$\phi_{\text{Zn}} = \phi_{\text{SHE}} - \left\{ \phi_{\text{SHE}}^\circ(\text{Zn}/\text{Zn}^{2+}) + \frac{RT}{z} \ln([\text{Zn}_{(\text{aq})}^{2+}]) \right\}, \quad (8)$$

where $\phi_{\text{SHE}}^{\circ}(\text{Zn}/\text{Zn}^{2+})$ is the standard electrode potential for the Zn/Zn^{2+} redox couple vs SHE (-0.762 V vs SHE [111]), $[\text{Zn}_{(\text{aq})}^{2+}]$ is the concentration of $\text{Zn}_{(\text{aq})}^{2+}$ in the electrolyte (considered as 1 M [23, 112]), and z is the number of electrons associated with the Zn/Zn^{2+} redox couple reaction ($z = 2$). Finally, the equation for Mn vacancy formation energy ($E_d(\text{V}_{\text{Mn}}^q)$) can be written as

$$\begin{aligned}
E_d(\text{V}_{\text{Mn}}^q, \Delta E_F, \phi_{\text{Zn}}) = & E_{\text{tot}}(\zeta(\text{V}_{\text{Mn}}^q)) - E_{\text{tot}}(\zeta(\text{host})) \\
& + \{\mu^{\circ}(\text{Mn}) + \Delta G^{\circ}(\text{Mn}_{(\text{aq})}^{2+}) + RT\ln([\text{Mn}_{(\text{aq})}^{2+}])\} \\
& + q\{E_{\text{VBE}}(\zeta(\text{host})) + \Delta E_F\} + E_{\text{corr}} \\
& - (2 + q)\{\phi_{\text{Zn}} + \phi_{\text{SHE}}^{\circ}(\text{Zn}/\text{Zn}^{2+})\},
\end{aligned} \tag{9}$$

A fork [113] of the PyDEF 2 [114, 115] code, which added compatibility with VASP 6, was used for the calculation of the formation energy of the defects. The CoFFEE code [116] was used for the calculation of the FNV correction, with the correction value incorporated into the results from PyDEF.

B. Experimental Methods

The pristine $\alpha\text{-MnO}_2$ active powder was supplied by Vibrantz Technologies and used without modification. Scanning electron microscopy (SEM) analysis of the pristine powder was performed and is presented in Fig. S1, with an average primary particle size of ca. 5 μm being seen. The cathodes were prepared in house by first creating a slurry 50% $\alpha\text{-MnO}_2$, 40% conductive carbon black and 10% polytetrafluoroethylene (PTFE) binder dissolved in a 2:1 mixture of Millipore Type I Ultra-pure water and isopropanol. This slurry was mixed using a planetary mixer (Mazerustar KK-250S) for 10 min at 900 rpm until a smooth and flowable slurry was achieved. It was then casted along the surface of the carbon paper current collector (AvCarb P50, AvCarb Materials Solutions) using a doctor blade with a 250 μm gap, then placed in an oven at 100 $^{\circ}\text{C}$ for a minimum of 3 h to allow for the water and isopropanol to fully evaporate. The resulting average active material loading was 0.80 mg cm^{-2} .

The experimental RAZIB cell was assembled using rectangular $\alpha\text{-MnO}_2$ electrodes cut using a custom die of dimensions 1.9 \times 3.0 cm with 2 mm radius corners. A similar die of

dimensions 2.0×3.1 cm was used to cut the glass microfiber separator (Whatman GF/D) and imprint the desired shape on to Zn metal foil, which was then cut out using scissors. The electrode assembly was placed into the bottom side of a cartridge cell designed for use in *in-situ* NMR experiments, as described previously [117, 118], with $710 \mu\text{L}$ of aqueous 1 M ZnSO_4 electrolyte being added. The cell was closed and rested overnight so that the cell is uniformly wetted prior to cycling. All RAZIB tests were conducted utilizing the cartridge cell setup just described.

The Mn dissolution process occurring during RAZIB cycling was probed through an analysis of the $\text{Mn}_{(\text{aq})}^{2+}$ concentration ($[\text{Mn}_{(\text{aq})}^{2+}]$) in the electrolyte captured by *operando* ^1H nuclear magnetic resonance (^1H NMR) experiments. All ^1H NMR spectroscopy measurements were carried out at an external magnetic field strength of 7.05 T, nominally 300.33 MHz for ^1H . The electrochemical cell was placed in a parallel plate resonator tuned to 300 MHz [119], which was connected to a Bruker MicWB40 probe. A Bruker Avance IIIHD spectrometer was used for collection of ^1H NMR data and all spectra were processed and plotted using Topspin. *Operando* ^1H NMR spectra were collected during cell cycling using a pulse-acquire sequence with a pulse tip angle of $\beta \approx 16^\circ$ and a repetition time of 0.9375 s. Sixty-four scans were acquired per 1D acquisition, resulting in a data collection time of 60 s for each *operando* ^1H NMR spectrum. *In situ* measurements of the H_2O T_1 relaxation time were acquired using an inversion recovery sequence and analyzed in Topspin using a two-component fit, as described recently [120]. The resulting fit was then used to determine the $[\text{Mn}_{(\text{aq})}^{2+}]$ in the cell electrolyte [120].

The *in situ* cell was placed in the ^1H NMR probe and attached to a Gamry Interface 1010E potentiostat for electrochemical cycling using the same setup as described previously [118, 120, 121]. The cell was discharged to 1.1 V using a current of 0.13 mA cm^{-2} (0.16 mA mg^{-2}), at which point the cell was rested for one hour under open circuit conditions so that the electrolyte could return to equilibrium. The *operando* ^1H NMR experiments were then halted and the *in situ* determination of $[\text{Mn}_{(\text{aq})}^{2+}]$ by analysis of the solvent T_1 was carried out. After completion of the T_1 determination, *operando* ^1H NMR measurements were simultaneously started while beginning to charge the cell. The cell was charged to 1.8 V using a current of 0.13 mA cm^{-2} and again allowed to rest for one hour prior to $[\text{Mn}_{(\text{aq})}^{2+}]$ measurement. The cell was then cycled symmetrically three times using the same currents without open-circuit voltage (OCV) holds and subsequently discharged, rested at

open circuit for ^1H NMR experiments, then charged similarly as before for ^1H NMR measurements after the fifth discharge and charge steps. This was repeated to obtain *in situ* T_1 measurements for cycles 10, 15, and 20 interleaved with *operando* ^1H NMR measurements during cycling. The percentage of Mn dissolved from the electrode was determined with respect to the initial mass of MnO_2 in the electrode, and then calculated by dividing the obtained $[\text{Mn}^{2+}_{(\text{aq})}]$ from the ^1H NMR measurement by the maximum $[\text{Mn}^{2+}_{(\text{aq})}]$ possible if all the active material had dissolved into the electrolyte.

III. RESULTS AND DISCUSSION

The supercell structures of $\alpha\text{-MnO}_2$ and $\alpha\text{-ZnMn}_2\text{O}_4$ after relaxation are shown in Fig. 1. The $\alpha\text{-MnO}_2$ structure is formed by 2×2 tunnels, with MnO_6 octahedra in two different orientations forming the tunnels (Fig. 1a). In the case of $\alpha\text{-ZnMn}_2\text{O}_4$, the intercalated Zn^{2+} ions established themselves within the tunnels, forming a bent coordination with the O atoms (ZnO_2), with the characteristic 2×2 tunnels from $\alpha\text{-MnO}_2$ being preserved (Fig. 1b). The Mn atoms in $\alpha\text{-MnO}_2$ can all be considered crystallographically equivalent due to their symmetry within the structure, despite the difference in the octahedral orientations in the tunnels. However, for the discharged structure $\alpha\text{-ZnMn}_2\text{O}_4$, the Mn atoms are not crystallographically equivalent anymore. The symmetry loss for the Mn atoms in $\alpha\text{-ZnMn}_2\text{O}_4$ is a result of the ZnO_2 bent coordination formed after the Zn^{2+} intercalation, which caused two crystallographically different Mn sites to be established. Therefore, it becomes necessary to differentiate the Mn atoms present in $\alpha\text{-ZnMn}_2\text{O}_4$ with respect to their orientation to the intercalated Zn atoms. The Mn atoms that have their MnO_6 octahedral orientation in the tunnel parallel to the ZnO_2 bent coordination are classified as Mn1 (olive-coloured atoms in Fig. 1b). Meanwhile, the Mn atoms with MnO_6 octahedral orientation perpendicular to the ZnO_2 coordination are labelled Mn2 (teal-coloured atoms in Fig. 1b). A complete analysis regarding the V_{Mn} formation in $\alpha\text{-ZnMn}_2\text{O}_4$ can then be expected after distinguishing between the two different Mn sites, as different results could be obtained for each site due to their crystallographic difference. The relaxed supercell structures of $\lambda\text{-MnO}_2$ and $\lambda\text{-ZnMn}_2\text{O}_4$ can be seen in Fig. S2 in the supplementary information (SI), with both materials retaining their cell symmetry and crystallographic equivalency for the Mn atom sites after relaxation.

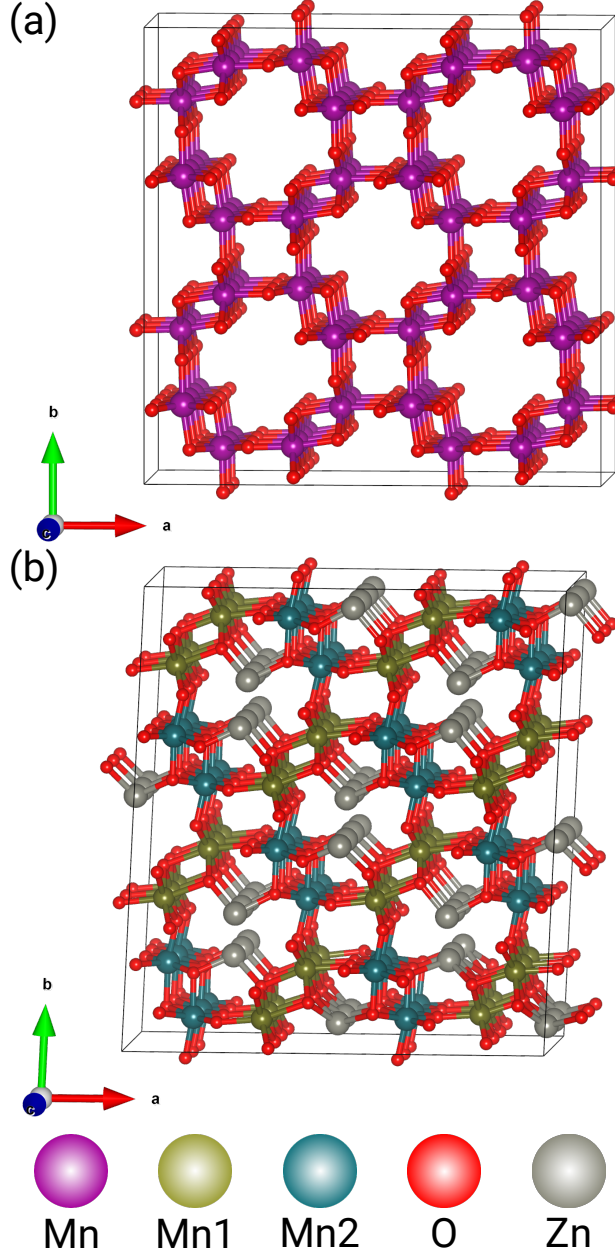


FIG. 1. Relaxed crystal structures of bulk (a) α -MnO₂ and (b) α -ZnMn₂O₄. As described in the text, the α -ZnMn₂O₄ Mn atoms have been classified as Mn1 (olive) or Mn2 (teal) depending on the orientation of their MnO₆ octahedral with respect to the bent coordination of the Zn atoms.

The positions of the Mn1 vacancy (V_{Mn1}) and Mn2 vacancy (V_{Mn2}) sites in α -ZnMn₂O₄ are presented in Fig. 2a, while in Figs. 2b and 2c the relaxed α -ZnMn₂O₄ structures for the neutral ($q=0$) V_{Mn1} and V_{Mn2} defects can be respectively seen. It was found from the atomic relaxation of α -ZnMn₂O₄(V_{Mn1}) that the lowest energy structure had the V_{Mn1} site occupied by a previously neighbouring Zn atom (Fig. 2b). The Zn atom now on the V_{Mn1}

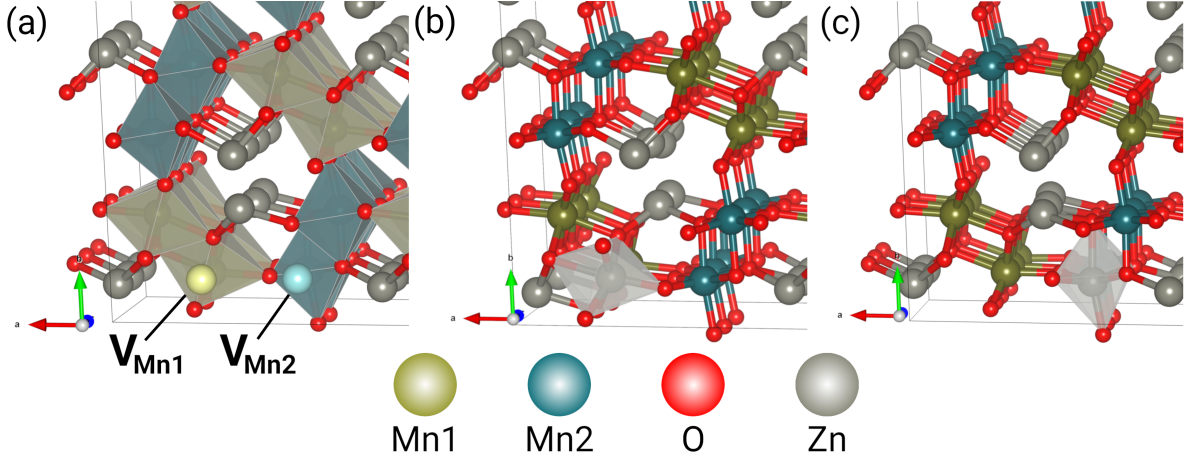


FIG. 2. (a) V_{Mn1} and V_{Mn2} sites position in the α -ZnMn₂O₄ crystal structure indicated by lighter shaded Mn1 and Mn2 atoms, respectively. Relaxed structures of (b) α -ZnMn₂O₄(V_{Mn1}) and (c) α -ZnMn₂O₄(V_{Mn2}) for neutral charge defects ($q = 0$), with the ZnO₆ octahedra established after relaxation highlighted as a polyhedron. Only a zoomed-in region of the respective simulated α -ZnMn₂O₄(V_{Mn}) cells is presented here to facilitate the visual analysis of the V_{Mn} positioning and atomic displacements during the relaxation of the Mn vacant structures.

site establishes an octahedral coordination with the oxygen atoms (ZnO₆), similarly to the Mn1 atom that formed the vacancy. The formation of ZnO₆ octahedral coordination at the V_{Mn} position was also observed in the relaxed α -ZnMn₂O₄(V_{Mn2}) structure (Fig. 2c). The structural transformation undergone by both α -ZnMn₂O₄(V_{Mn}) structures can be understood as a Zn substitution reaction, with the previously intercalated Zn atom replacing the Mn atom in the octahedral after the Mn vacancy is formed and Mn is dissolved into the electrolyte. The shift in Zn coordination during the relaxation of the vacant structure potentially indicates that the bent Zn coordination established after intercalation is energetically unstable, with a more stable octahedral coordination only structurally possible to be formed after the Mn atom dissolution. A more detailed analysis of the impact of the structural transformations undergone by α -ZnMn₂O₄(V_{Mn}) on the propensity for Mn dissolution from the structure is presented later, alongside the discussion of the calculated $E_d(V_{Mn}^q)$ for the material. In the case of α -MnO₂(V_{Mn}), λ -MnO₂(V_{Mn}), and λ -ZnMn₂O₄(V_{Mn}), negligible structural transformations were observed after relaxation (see Figs. S3b, S4b and S4d in the SI).

First, the neutral Mn vacancy formation energy ($E_d(V_{Mn}^0)$) ($q = 0$) was calculated for all the materials considering an electrode potential equal to 0 V vs SHE ($\phi_{Zn} = 0.762$ V vs Zn/Zn²⁺ in Eq. (9)), and is shown in Table I. An electrode potential of 0 V vs SHE was chosen here

TABLE I. Results for the neutral Mn vacancy formation energy ($E_d(V_{\text{Mn}}^0)$) and Mn vacancy formation energy for a $q = -2$ charged defect at the conduction band edge ($E_d(V_{\text{Mn}}^{-2}, \text{CBE})$) for the MnO_2 and ZnMn_2O_4 polymorphs, alongside the supporting parameters: cell relaxation energy variation for neutral Mn vacancy ($\Delta E_{\text{rlx}}(V_{\text{Mn}}^0)$) and neutral Mn vacancy formation energy without relaxation ($E_d(V_{\text{Mn}}^0)_{\text{wor}}$) (described in the text). All values are in eV. At the conditions investigated in this paper, an electrode potential of 0.762 V vs Zn/Zn^{2+} is equivalent to 0 V vs SHE (see Eq. (8)). Results for $\alpha\text{-ZnMn}_2\text{O}_4$ are presented with respect to $\text{V}_{\text{Mn}1} / \text{V}_{\text{Mn}2}$ sites. The Mn-vacant structures before and after relaxation are presented in Figs. S6 and S7 in the SI.

Property	ϕ_{Zn} (V vs Zn/Zn^{2+})	α		λ	
		MnO_2	ZnMn_2O_4	MnO_2	ZnMn_2O_4
$E_d(V_{\text{Mn}}^0)$	0.762	6.9	-0.1 / 0.2	7.9	3.0
$\Delta E_{\text{rlx}}(V_{\text{Mn}}^0)$	-	-1.0	-4.1 / -4.9	-0.1	-1.9
$E_d(V_{\text{Mn}}^0)_{\text{wor}}$	0.762	7.9	4.0 / 5.1	8.0	4.9
$E_d(V_{\text{Mn}}^{-2}, \text{CBE})$	-	5.4	-0.1 / 0.2	4.4	1.7
$E_d(V_{\text{Mn}}^0)$	1.8	4.8	-2.1 / -1.9	5.8	0.9
$E_d(V_{\text{Mn}}^0)$	1.1	6.2	-0.7 / -0.5	7.2	2.3

because it allows for a direct comparison to previously reported $E_d(V_{\text{Mn}}^0)$ results for Mn oxides. The high $E_d(V_{\text{Mn}}^0)$ values seen for both MnO_2 polymorphs (7 eV or higher) display how energetically unfavourable the V_{Mn} formation and subsequent dissolution as $\text{Mn}_{\text{(aq)}}^{2+}$ would be in both structures. Similar Mn vacancy formation calculations were previously performed for different MnO_2 polymorphs, with formation energies greater than 10 eV being reported [122, 123]. The disparity between our results and previous reports can be ascribed to the difference in chemical environment considered for the Mn atom in the $E_d(V_{\text{Mn}}^0)$ calculation, which was here taken as $\text{Mn}_{\text{(aq)}}^{2+}$ (see Eqs. (5), (6) and (7)). For example, Young *et al.* [122] calculated a $E_d(V_{\text{Mn}}^0)$ in $\alpha\text{-MnO}_2$ to be of approximately 11 eV when considering a Mn chemical environment that of $\text{Mn}_{\text{(s)}}^0$ (Mn-rich environment) and without performing defective cell relaxation. The $E_d(V_{\text{Mn}}^0)$ result by Young *et al.* [122] can then be adjusted to be with respect to $\text{Mn}_{\text{(aq)}}^{2+}$ (Eqs. (6) and (7)), resulting in a $E_d(V_{\text{Mn}}^0)$ of approximately 8.6 eV, which is similar to our results for MnO_2 polymorphs without relaxation (Table I). Overall, all studies agree that the formation of a V_{Mn} is energetically highly unfavourable, independent of the MnO_2 polymorph considered; thus, it is expected that the Mn atom will remain in the MnO_2 lattice.

A considerably lower $E_d(V_{\text{Mn}}^0)$ value is observed for the vacancy in both ZnMn_2O_4 struc-

tures. For example, in the λ polymorph a reduction of 4.9 eV on the neutral Mn vacancy (V_{Mn}^0) formation energy is observed after the inclusion of Zn atoms in the λ - MnO_2 spinel structure (see Table I). Yet, the calculated $E_d(V_{\text{Mn}}^0)$ in λ - ZnMn_2O_4 is still considerably high, which would also restrain the Mn dissolution as $\text{Mn}_{(\text{aq})}^{2+}$ from the structure. However, drastically lower $E_d(V_{\text{Mn}}^0)$ values were found for α - ZnMn_2O_4 , with even negative $E_d(V_{\text{Mn}}^0)$ values being established for the $\text{V}_{\text{Mn}1}$ formation. The negative $E_d(V_{\text{Mn}}^0)$ result indicates the energetic feasibility for $\text{V}_{\text{Mn}1}$ formation in α - ZnMn_2O_4 at an electrode potential of 0.762 V vs Zn/Zn^{2+} (equivalent to 0 V vs SHE), demonstrating that the Mn atoms become more prone to dissolution as $\text{Mn}_{(\text{aq})}^{2+}$ once the α - ZnMn_2O_4 structure is formed. Therefore, the $E_d(V_{\text{Mn}}^0)$ results indicate that the Zn^{2+} intercalation process occurring during discharge would prompt the transition from an electrochemically stable α - MnO_2 structure in the electrode to an unstable α - ZnMn_2O_4 phase, from which the Mn atoms would then dissolve into the electrolyte. The electrochemical instability and associated tendency for Mn dissolution from α - ZnMn_2O_4 under RAZIB operation conditions is discussed later in this section.

Now, it is important to understand why the $E_d(V_{\text{Mn}}^0)$ is considerably lower for the ZnMn_2O_4 structures with respect to their respective MnO_2 polymorphs. In order to answer this question, we have performed self-consistent (SC) calculations for the structures containing V_{Mn}^0 before and after relaxation to quantify the impact of the structural transformations occurring during relaxation on the calculated $E_d(V_{\text{Mn}}^0)$. The cell relaxation energy variation for neutral Mn vacancy ($\Delta E_{\text{rlx}}(V_{\text{Mn}}^0)$) is a new parameter established in this work to aid in the $E_d(V_{\text{Mn}}^0)$ analysis, capturing the change in the total energy of the vacant system before and after relaxation. $\Delta E_{\text{rlx}}(V_{\text{Mn}}^0)$ allows for the quantification of the energy reduction in the V_{Mn}^0 -containing system due to the structural transformations undergone during relaxation. By subtracting $\Delta E_{\text{rlx}}(V_{\text{Mn}}^0)$ from $E_d(V_{\text{Mn}}^0)$, it is also possible to calculate the neutral Mn vacancy formation energy without relaxation ($E_d(V_{\text{Mn}}^0)_{\text{wor}} = E_d(V_{\text{Mn}}^0) - \Delta E_{\text{rlx}}(V_{\text{Mn}}^0)$), which is the associated V_{Mn}^0 formation energy if no atomic relaxation was performed for the vacant structure. A configuration energy diagram demonstrating the relationship between $E_d(V_{\text{Mn}}^0)$, $E_d(V_{\text{Mn}}^0)_{\text{wor}}$, and $\Delta E_{\text{rlx}}(V_{\text{Mn}}^0)$ is presented in Fig. S5. The $\Delta E_{\text{rlx}}(V_{\text{Mn}}^0)$ and $E_d(V_{\text{Mn}}^0)_{\text{wor}}$ values calculated for all materials are also shown in Table I, while the V_{Mn}^0 -containing structures before and after relaxation are presented in Figs. S6 and S7 in the SI.

The $E_d(V_{\text{Mn}}^0)_{\text{wor}}$ results revealed the existence of a common V_{Mn}^0 formation energy only

dependent on the chemistry of the system, as both MnO_2 structures report a high $E_d(\text{V}_{\text{Mn}}^0)_{\text{wor}}$ value of approximately 8 eV, while the ZnMn_2O_4 counterparts have a lower formation energy of about 5 eV. In order to understand the difference between the $E_d(\text{V}_{\text{Mn}}^0)_{\text{wor}}$ results in MnO_2 and ZnMn_2O_4 it is necessary to examine the variation in electron availability due to the presence of a V_{Mn}^0 . The formation of a V_{Mn}^0 will cause a reduction in the number of electrons available in the structure for the atoms to establish their preferential oxidation states. The higher the oxidation state is prior to the vacancy formation, the harder it will be for the atoms to accommodate the electron loss, since more electrons were previously participating in establishing the bonds in the structure. Therefore, the high Mn oxidation state in MnO_2 (Mn^{4+}) will make the V_{Mn}^0 formation less favourable (higher $E_d(\text{V}_{\text{Mn}}^0)_{\text{wor}}$) than in ZnMn_2O_4 (Mn^{3+}), as there will be a lower number of electrons available in the vacant structure for the Mn to maintain the considerably high 4+ oxidation state. In order to verify the proposed relationship between oxidation state and $E_d(\text{V}_{\text{Mn}}^0)_{\text{wor}}$, the formation of a V_{Mn}^0 was also investigated for MnO (Mn^{2+}) and Mn_2O_3 (Mn^{3+}). The $E_d(\text{V}_{\text{Mn}}^0)_{\text{wor}}$ results for different Mn oxidation states is presented in Fig. S8, where a clear trend is established between the results for the binary Mn oxides (*i.e.*, MnO , Mn_2O_3 and MnO_2) and ZnMn_2O_4 , showing that the higher the Mn oxidation state, the higher the $E_d(\text{V}_{\text{Mn}}^0)_{\text{wor}}$ is, and that Mn atoms with the same oxidation state (in this case Mn^{3+}) indeed have similar $E_d(\text{V}_{\text{Mn}}^0)_{\text{wor}}$ results. Finally, the same trend between oxidation state and $E_d(\text{V}_{\text{Mn}}^0)_{\text{wor}}$, as discussed here for Mn, can also be expected for the vacancy formation of other elements in other chemical systems, since the rationale behind the trend is independent of the Mn oxide chemistry being studied here. For example, the observed trend can be directly applied for screening new stable cathode materials for batteries, as materials with redox-active atoms at higher oxidation state will be less prone to dissolution during cycling.

The $E_d(\text{V}_{\text{Mn}}^0)_{\text{wor}}$ base values calculated for MnO_2 (ca. 8 eV) and ZnMn_2O_4 (ca. 5 eV) can then be interpreted as the upper limit for the V_{Mn}^0 formation energy in the respective materials, as the chemistry was shown to be the primary parameter governing the vacancy formation energy when relaxation is not considered. Then, it is possible to conclude that the ZnMn_2O_4 structures are invariably more prone to Mn dissolution than the respective MnO_2 polymorph due to a lower Mn oxidation state established after Zn^{2+} intercalation. Similar results can be expected for cathode materials in other battery chemistries, with a lower vacancy formation energy being found for the discharged phase (*i.e.*, higher propen-

sity for active material dissolution) than for the charged phase due to the reduction in transition metal oxidation state after ionic intercalation. Once relaxation is performed, the vacancy formation energy universally decreases, but by different magnitudes, which causes materials with the same chemistry to then have noticeably distinct $E_d(V_{\text{Mn}}^0)$ depending on their structure (see Table I). The impact of relaxation on the calculated $E_d(V_{\text{Mn}}^0)$ can be clearly seen from the results for different polymorphs of ZnMn_2O_4 , as a considerable energy reduction due to the structural transformations undergone during relaxation was observed for $\alpha\text{-ZnMn}_2\text{O}_4(V_{\text{Mn}})$ (calculated $|\Delta E_{\text{rlx}}(V_{\text{Mn}}^0)|$ greater than 4 eV). As previously discussed, the major structural transformation observed after the relaxation of $\alpha\text{-ZnMn}_2\text{O}_4(V_{\text{Mn}})$ structures is a shift in Zn coordination from bent (ZnO_2) to octahedral (ZnO_6), with the Zn atom substituting the dissolved Mn atom on the V_{Mn} site (see Fig. 2b,c).

A question then arises: how can a change in coordination of a single Zn atom in $\alpha\text{-ZnMn}_2\text{O}_4(V_{\text{Mn}})$ be responsible for an energy decrease from cell relaxation ($\Delta E_{\text{rlx}}(V_{\text{Mn}}^0)$) of more than 4 eV? To answer this question it is necessary to look into the energetically favourable coordination environments for Zn in solid materials. A literature survey reveals that Zn atoms are preferably coordinated tetrahedrally ($\text{Zn}X_4$, e.g., Sphalerite / Wurtzite (ZnS), Zincite (ZnO), Hemimorphite ($\text{Zn}_4\text{Si}_2\text{O}_7(\text{OH})_2 \cdot \text{H}_2\text{O}$), Willemite (Zn_2SiO_4)) or octahedrally ($\text{Zn}X_6$, e.g., Smithsonite (ZnCO_3), Hopeite ($\text{Zn}_3(\text{PO}_4)_2$)) in naturally occurring inorganic materials [124–126]. The energetic preference for tetrahedral or octahedral Zn coordinations can be ascribed to the complete filling of the degenerate t_{2g} and e_g states in the *d*-block molecular orbitals for both coordinations by the Zn^{2+} d^{10} electrons [127]. In the case of $\lambda\text{-ZnMn}_2\text{O}_4(V_{\text{Mn}})$, the Zn atoms are already at an energetically favourable tetrahedral coordination in the V_{Mn} -free structure (see Fig. S2b), which will cause for the material to have a lower $\Delta E_{\text{rlx}}(V_{\text{Mn}}^0)$ since no considerable structural transformations are energetically favourable to occur. A $\lambda\text{-ZnMn}_2\text{O}_4(V_{\text{Mn}})$ cell with a Zn atom octahedrally coordinated in the V_{Mn} site was also investigated, with negligible change in energy with respect to the tetrahedral Zn coordination being found (< 50 meV). However, in $\alpha\text{-ZnMn}_2\text{O}_4$, the Zn atoms are in a bent coordination (ZnO_2), which, according to the literature [124–126], is an energetically unfavourable chemical environment for the Zn atoms when compared to the octahedral and tetrahedral coordinations. Therefore, with the formation of a V_{Mn} in $\alpha\text{-ZnMn}_2\text{O}_4$ the Zn atom can shift from a bent to an octahedral coordination in the structure, greatly reducing the energy of the system (high $|\Delta E_{\text{rlx}}(V_{\text{Mn}}^0)|$), and consequently granting

a considerably low $E_d(V_{\text{Mn}}^0)$ for the $\alpha\text{-ZnMn}_2\text{O}_4(V_{\text{Mn}})$ structures.

The local potential (U_{local}) for the $\alpha\text{-ZnMn}_2\text{O}_4(V_{\text{Mn}})$ structures before and after relaxation was also calculated in order to understand possible driving factors promoting the change in Zn atom coordination. The U_{local} analysis display the regions inside the V_{Mn}^0 -containing supercell where potential energy is concentrated, allowing for the visualization of regions that would be energetically favourable for ions to migrate towards during relaxation. In the DFT calculation, all properties are calculated with respect to the electron from the resulting electron density arrangement in the material. For this reason, a positive U_{local} concentration would be attractive for positively charged species (*e.g.*, Zn^{2+}) and a negative U_{local} concentration for negatively charged species (*e.g.*, e^-). The U_{local} is calculated at each point in the 3D real-space grid; therefore, to facilitate the visualization of cell regions with local potential concentration, it is necessary to determine a minimum cutoff value for the U_{local} points to be displayed. The calculated U_{local} presented here considers only the ionic and Hartree potentials (LVHAR=.TRUE. tag). The resulting volumetric regions for which $U_{\text{local}} > 10$ eV in both $\alpha\text{-ZnMn}_2\text{O}_4(V_{\text{Mn}})$ structures before and after relaxation are shown in Fig. 3. A U_{local} concentration around the V_{Mn} site can be clearly seen in both $\alpha\text{-ZnMn}_2\text{O}_4(V_{\text{Mn}})$ structures before performing cell relaxation (Fig. 3a,b), indicating that the empty V_{Mn} site is attractive for a Zn^{2+} cation. A Zn^{2+} ion then octahedrally coordinates at the V_{Mn} site once the relaxation is conducted, with a region of a high U_{local} being established on the site previously occupied by the Zn^{2+} , as expected (Fig. 3c,d). Therefore, the positive U_{local} concentration on the V_{Mn} site is responsible for attracting the bent coordinated Zn^{2+} ion in $\alpha\text{-ZnMn}_2\text{O}_4(V_{\text{Mn}})$ to the V_{Mn} site, with the established octahedral coordination causing for the energy of the system to be greatly reduced (high $|\Delta E_{\text{rlx}}(V_{\text{Mn}}^0)|$). A similar U_{local} analysis was also performed for $\alpha\text{-MnO}_2(V_{\text{Mn}})$, $\lambda\text{-MnO}_2(V_{\text{Mn}})$, and $\lambda\text{-ZnMn}_2\text{O}_4(V_{\text{Mn}})$, with negligible variations in U_{local} being observed before and after relaxation (see Fig. S9)

The formation of charged V_{Mn} defects ($q = -2$) was also investigated in all oxide structures, with the charged defect formation energy calculated from Eq. (9). The results for the $E_d(V_{\text{Mn}}^q)$ as function of the Fermi energy (E_F) are presented in Fig. S10. For all materials, except $\alpha\text{-ZnMn}_2\text{O}_4(V_{\text{Mn}})$, the transition energy level between the neutral and negatively charged V_{Mn} formation was calculated to be within the band gap for the respective host structures. The neutral to charged V_{Mn} transition energy level in $\alpha\text{-ZnMn}_2\text{O}_4$ was established for both Mn1 and Mn2 sites at the E_F of the host structure (Fig. S10b), as expected

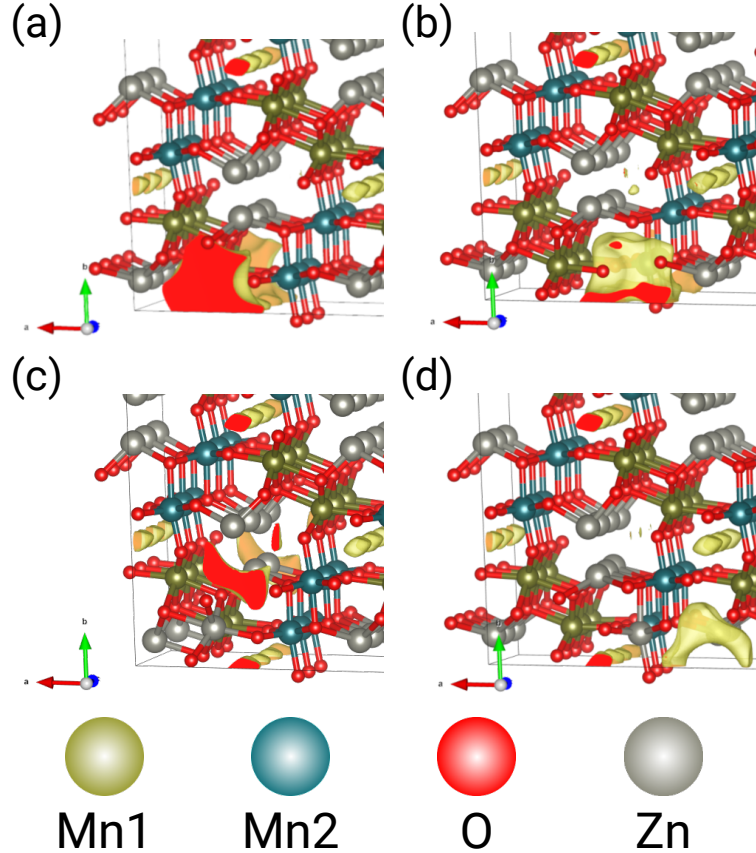


FIG. 3. (a,c) α -ZnMn₂O₄(V_{Mn1}) and (b,d) α -ZnMn₂O₄(V_{Mn2}) structures (a,b) before and (c,d) after atomic relaxation, featuring the regions of $U_{\text{local}} > 10$ eV in each structure.

for a material with a metallic character. Lower $E_d(V_{\text{Mn}}^q)$ values than the one calculated for V_{Mn}⁰ can be attained for both the α - and λ -MnO₂, depending upon the position of ΔE_F . The lowest $E_d(V_{\text{Mn}}^q)$ would be at the conduction band edge (CBE) for both α -MnO₂(V_{Mn}) and λ -MnO₂(V_{Mn}), with the $E_d(V_{\text{Mn}}^{-2}, \text{CBE})$ results for all materials also being shown in Table I. It is important to note that even the lowest $E_d(V_{\text{Mn}}^q)$ results found for the MnO₂ structures are still significantly high (greater than 4 eV), clearly demonstrating how energetically unfavourable the formation of a V_{Mn} in MnO₂ is. Similar conclusions can also be reached for the formation of a V_{Mn} in λ -ZnMn₂O₄, since the lowest calculated $E_d(V_{\text{Mn}}^q)$, also at the CBE, is still higher than 1.5 eV (see Table I). The transition level between neutral and charged V_{Mn} for α -ZnMn₂O₄ being established at the E_F leads to the $E_d(V_{\text{Mn}}^q)$ value for α -ZnMn₂O₄(V_{Mn}) being independent of the defect charge state considered ($E_d(V_{\text{Mn}}^0) = E_d(V_{\text{Mn}}^{-2}, \text{CBE})$), as shown in Table I. In conclusion, the higher propensity for Mn dissolution in the α -ZnMn₂O₄ structure than in the other oxides evaluated is still validated after

TABLE II. Reversible electrode potential for V_{Mn}^0 formation ($\phi_{\text{Zn}}^{\text{rev}}(V_{\text{Mn}}^0)$) in V vs Zn/Zn²⁺ for the MnO₂ and ZnMn₂O₄ polymorphs. Results for α -ZnMn₂O₄ are presented with respect to V_{Mn1} / V_{Mn2} sites.

Property	α		λ	
	MnO ₂	ZnMn ₂ O ₄	MnO ₂	ZnMn ₂ O ₄
$\phi_{\text{Zn}}^{\text{rev}}(V_{\text{Mn}}^0)$	4.2	0.7 / 0.8	4.7	2.2

considering the formation of charged V_{Mn} defects.

The applied electrode potential continuously varies during battery cycling, which directly impacts the calculated V_{Mn}⁰ formation energy for each material (see Eq. (9)). Therefore, to determine the energetic feasibility for Mn dissolution from each phase during battery operation it is necessary to consider the potential window relevant for RAZIB cycling. When $E_d(V_{\text{Mn}}^0)$ is equal to 0 eV, the Mn vacancy formation is in an energetic equilibrium, with the associated electrode potential being the reversible electrode potential for V_{Mn}⁰ formation ($\phi_{\text{Zn}}^{\text{rev}}(V_{\text{Mn}}^0)$). Also, according to Eq. (9), if the ϕ_{Zn} is higher than $\phi_{\text{Zn}}^{\text{rev}}(V_{\text{Mn}}^0)$, the V_{Mn}⁰ defect formation is energetically viable ($E_d(V_{\text{Mn}}^0) < 0$ eV, Mn is predicted to dissolve as Mn_(aq)²⁺, oxidation reaction in Eqs. (3) and (4)). And, if ϕ_{Zn} is lower than $\phi_{\text{Zn}}^{\text{rev}}(V_{\text{Mn}}^0)$ the V_{Mn}⁰ defect is not predicted to form ($E_d(V_{\text{Mn}}^0) > 0$ eV, Mn is not predicted to dissolve and remains on the cathode, reduction reaction in Eqs. (3) and (4)). The calculated $\phi_{\text{Zn}}^{\text{rev}}(V_{\text{Mn}}^0)$ values for each material is then presented on Table II. For α -MnO₂, λ -MnO₂, and λ -ZnMn₂O₄, it is predicted that the V_{Mn}⁰ formation will be energetically unfeasible to occur throughout the MnO₂ cathode RAZIB potential cycling window (from 1.1 to 1.8 V vs Zn/Zn²⁺ [14, 23]), since the battery would only cycle at potentials lower than the calculated $\phi_{\text{Zn}}^{\text{rev}}(V_{\text{Mn}}^0)$. However, in the case of α -ZnMn₂O₄, a considerably lower $\phi_{\text{Zn}}^{\text{rev}}(V_{\text{Mn}}^0)$ was calculated for both Mn1 and Mn2 sites (see Table II). The $\phi_{\text{Zn}}^{\text{rev}}(V_{\text{Mn}}^0)$ around 0.8 V vs Zn/Zn²⁺ calculated for α -ZnMn₂O₄ indicates that the dissolution of Mn atoms as Mn_(aq)²⁺ will be thermodynamically favourable throughout the potential window for RAZIB cycling. The same conclusion of V_{Mn} formation in α -ZnMn₂O₄ throughout the RAZIB cycling can be reached from the negative $E_d(V_{\text{Mn}}^0)$ results at the cycling boundary potentials presented in Table I. Therefore, it is predicted that at discharge, where α -ZnMn₂O₄ is the primary phase in the electrode, Mn vacancies will be energetically favourable to form, consequently increasing the concentration of Mn_(aq)²⁺ in the electrolyte.

From the analysis of the $E_d(V_{\text{Mn}}^0)$ results at relevant RAZIB cycling potentials, it is possible to ascribe the proneness for Mn dissolution from $\alpha\text{-MnO}_2$ cathodes during cycling to the unstable Zn coordination established during intercalation. The conclusion for Mn dissolution promoted by unstable Zn coordination on the structure can be arrived from the analysis of the structural transformations undergone by $\alpha\text{-ZnMn}_2\text{O}_4(V_{\text{Mn}})$ during relaxation, which have been shown to drastically reduce the $E_d(V_{\text{Mn}}^0)$ for the phase (high $|\Delta E_{\text{rlx}}(V_{\text{Mn}}^0)|$) and ultimately contribute for $\alpha\text{-ZnMn}_2\text{O}_4(V_{\text{Mn}})$ to have negative $E_d(V_{\text{Mn}}^0)$ throughout the RAZIB cycling window. The Mn dissolution mechanism based on unstable Zn coordination occurring during RAZIB operation can be described as follow. During discharge, Zn^{2+} ions intercalate into the electrode and establish themselves with an unstable bent coordination on the $\alpha\text{-MnO}_2$ tunnelled structure. The unstable Zn coordination on the structure severely reduces the energy for Mn dissolution by promoting a substitution reaction, with a Mn atom dissolving into the electrolyte as $\text{Mn}_{(\text{aq})}^{2+}$ while a Zn atom establishes an octahedral coordination on the vacant Mn site.

It is important to note that the Mn dissolution mechanism described here may not be unique to $\alpha\text{-MnO}_2$ electrodes for RAZIBs, since what causes the Mn dissolution to become energetically favourable is the presence of an unstable coordination environment, which can potentially occur in different cathodes and battery chemistries. Also, the impact of unstable Zn coordination for promoting the Mn dissolution in the tunnelled $\alpha\text{-MnO}_2$ structure highlights the importance of considering the intercalating ion coordination environment to the host structure, and not only the available space for ionic diffusion, when exploring novel cathode materials for RAZIB and other battery chemistries. For example, MnO_2 polymorphs with wider tunnels than $\alpha\text{-MnO}_2$, such as Romanèchite- MnO_2 (2×3 tunnels) and Todorokite- MnO_2 (3×3 tunnels), will also be susceptible to the unstable Zn coordination Mn dissolution mechanism being proposed here, since a favourable Zn coordination environment is also not expected to be established in the structures due to the extensive tunnel space. Therefore, by considering the effect of unstable coordination of intercalating ions on the electrode material stability under operation conditions, a more rational design of cathode materials to support the ongoing energy transition can be expected.

So far, the formation of the V_{Mn} has only been investigated for the two extreme battery compositions, the completely charged (MnO_2) and discharged (ZnMn_2O_4) phases. However, the composition, and consequently structure, of the initially $\alpha\text{-MnO}_2$ electrode is actively

changing during battery cycling, which will then cause for the $E_d(V_{\text{Mn}}^0)$ of the electrode to also vary during cycling. Therefore, it is necessary to capture both the phase present in the electrode and the applied potential in order to accurately model the $E_d(V_{\text{Mn}}^0)$ of the electrode. Considering a rocking chair battery model [128], the major phase present in the electrode at high potentials will be the completely charged phase of $\alpha\text{-MnO}_2$. And during discharge, capacity will be gained by having Zn^{2+} intercalating into the electrode, with the Zn content in $\alpha\text{-Zn}_x\text{Mn}_2\text{O}_4$ increasing until the completely discharged phase $\alpha\text{-ZnMn}_2\text{O}_4$ is established. The $\alpha\text{-Zn}_x\text{Mn}_2\text{O}_4$ phase present on the electrode can then be actively tracked with respect to the capacity being gained on the electrode, with x considered to be equal to 0 at the top of charge (*i.e.*, $\alpha\text{-MnO}_2$) and 1 at the bottom of discharge (*i.e.*, $\alpha\text{-ZnMn}_2\text{O}_4$). The $E_d(V_{\text{Mn}}^0)$ for the electrode was then calculated through a linear interpolation of the $E_d(V_{\text{Mn}}^0)$ results for $\alpha\text{-MnO}_2(V_{\text{Mn}})$, $\alpha\text{-Zn}_{0.5}\text{Mn}_2\text{O}_4(V_{\text{Mn}})$, and $\alpha\text{-ZnMn}_2\text{O}_4(V_{\text{Mn}1})$ with respect to the experimental ϕ_{Zn} and capacity gained for an $\alpha\text{-MnO}_2$ electrode. A partially discharged $\alpha\text{-Zn}_{0.5}\text{Mn}_2\text{O}_4$ ($x = 0.5$) structure was also considered in order to more accurately capture the $E_d(V_{\text{Mn}}^0)$ profile for the electrode during cycling, with the initial $\alpha\text{-Zn}_{0.5}\text{Mn}_2\text{O}_4$ structure being created by randomly removing Zn atoms from the $\alpha\text{-ZnMn}_2\text{O}_4$ structure.

The predicted $E_d(V_{\text{Mn}}^0)$ for the electrode during battery cycling is shown in Fig. 4, alongside the experimental galvanostatic charge/discharge (GCD) profile for a RAZIB cell with an $\alpha\text{-MnO}_2$ cathode. As explained previously, multiple reports rely on the JTE-assisted charge disproportionation reaction from ZnMn_2O_4 to explain the Mn dissolution in $\alpha\text{-MnO}_2$ RAZIB cathodes as $\text{Mn}_{(\text{aq})}^{2+}$ [19, 48, 51, 53–57]. However, our results for the electrode $E_d(V_{\text{Mn}}^0)$ show that the Mn dissolution is already predicted to be thermodynamically feasible before the battery is fully discharged and the $\alpha\text{-ZnMn}_2\text{O}_4$ phase is completely formed, as the $E_d(V_{\text{Mn}}^0)$ results for a partially discharged cell ($x < 0.5$) are already negative. Therefore, there is a slight discrepancy between our results and previous literature that pointed towards the JTE-assisted charge disproportionation reaction as the driving mechanism for the Mn dissolution. In order to uncover the dissolution dynamics during battery cycling, the $[\text{Mn}_{(\text{aq})}^{2+}]$ on the electrolyte was quantified during cycling of a RAZIB cell with $\alpha\text{-MnO}_2$ cathode utilizing *operando* ^1H NMR [120]. In the ^1H NMR experiments, the ^1H signal chemical shift and its associated recovery time are directly related to the $[\text{Mn}_{(\text{aq})}^{2+}]$ in the battery electrolyte, with peaks changes to higher chemical shifts indicating higher $[\text{Mn}_{(\text{aq})}^{2+}]$ (see Sec. II B)[120].

The ^1H NMR experiments revealed that Mn dissolution starts occurring at the beginning

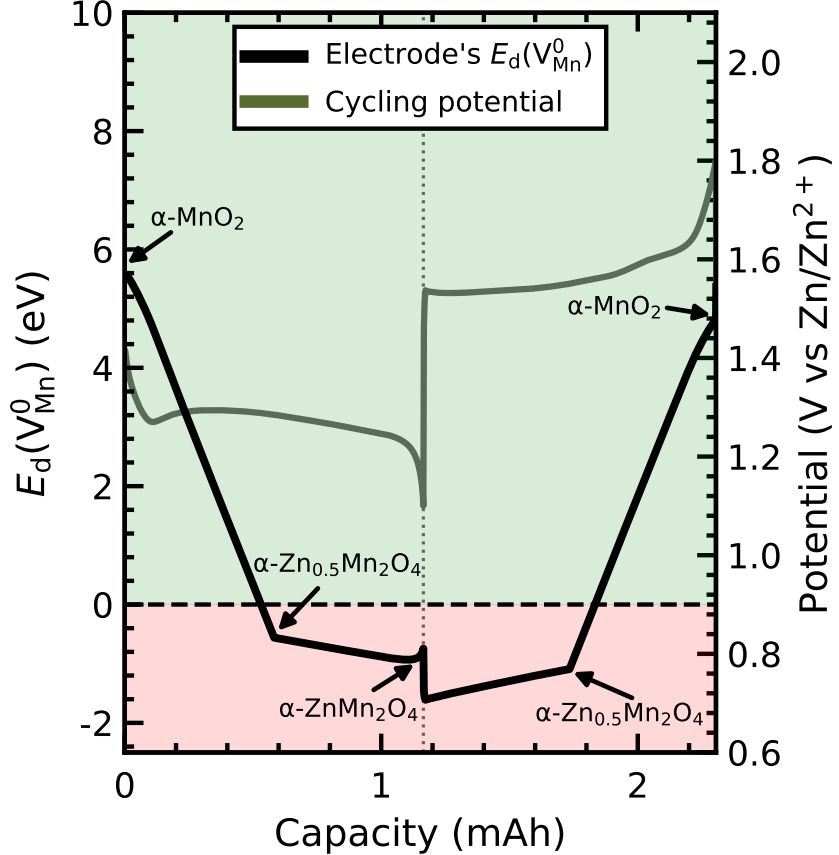


FIG. 4. The neutral Mn vacancy formation energy ($E_d(V_{\text{Mn}}^0)$) for the electrode calculated with respect to the $\alpha\text{-MnO}_2$ cathode galvanostatic charge/discharge (GCD) experiment result (initial active material loading equal to 4.5 mg). The experimental GCD cycling potential profile used for calculating $E_d(V_{\text{Mn}}^0)$ is also shown in the figure on a secondary axis. The green and red regions highlight the $E_d(V_{\text{Mn}}^0)$ results for which the Mn dissolution is respectively thermodynamically unfavourable ($E_d(V_{\text{Mn}}^0) > 0$ eV) and favourable ($E_d(V_{\text{Mn}}^0) < 0$ eV). The specific capacity shown in the figure is the accumulated specific capacity expended and restored through the discharge and charge cycles. The arrows present in the graph highlight the positions in the $E_d(V_{\text{Mn}}^0)$ curve for the electrode where the $\alpha\text{-MnO}_2$, $\alpha\text{-Zn}_{0.5}\text{Mn}_2\text{O}_4$, and $\alpha\text{-ZnMn}_2\text{O}_4$ phases are considered to be constituting the electrode.

of the discharge cycle and continues throughout the entire $\alpha\text{-MnO}_2$ cathode discharge, as captured by the increase in chemical shift for the ^1H peak during battery discharge shown in Fig. 5a. The increase in $[\text{Mn}_{(\text{aq})}^{2+}]$ in the electrolyte at the beginning of the battery discharge, where low concentrations of Zn^{2+} ions have intercalated into the structure, indicates the formation of a slightly discharged phase from which Mn dissolution is already energetically favourable. Therefore, the ^1H NMR results are in agreement with our theoretical calculations, and the proposed unstable Zn coordination dissolution mechanism, which predicted

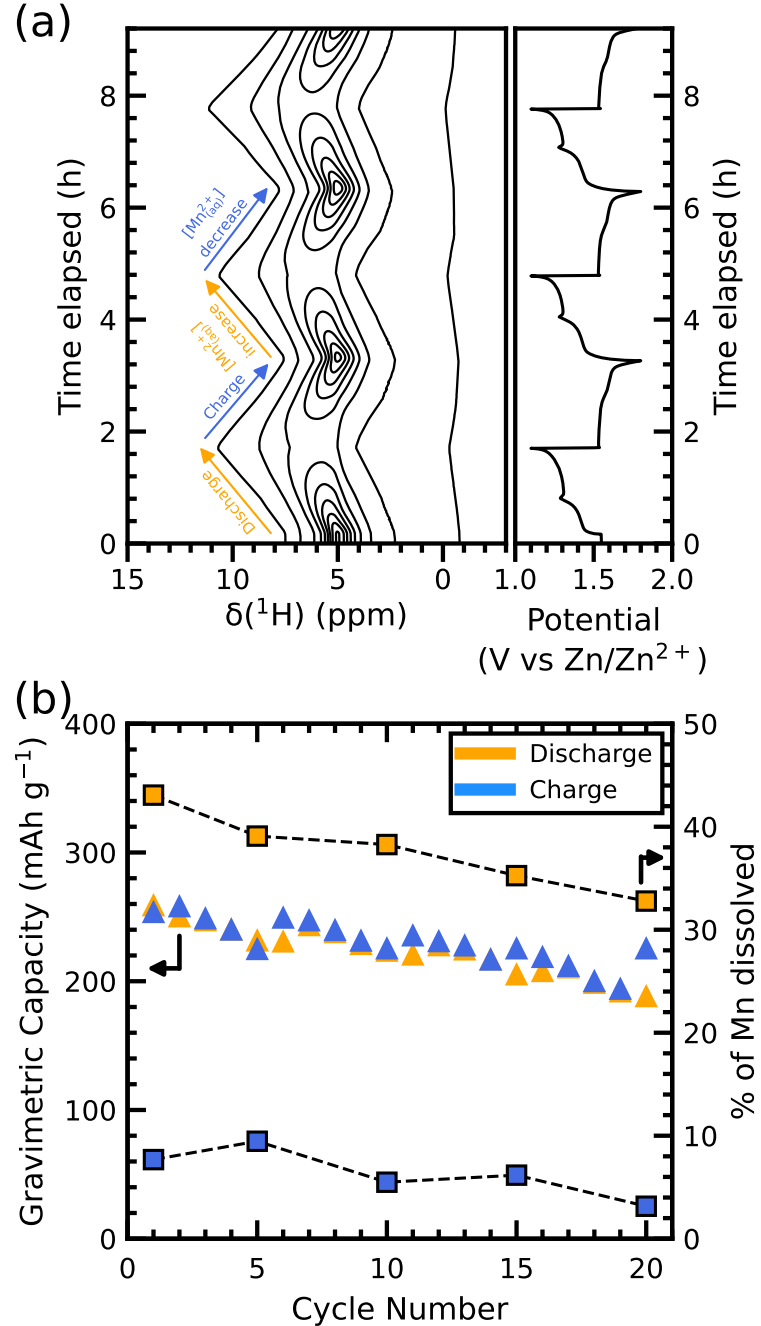


FIG. 5. (a) Contour plot for chemical shift peak intensity during *operando* ¹H nuclear magnetic resonance (¹H NMR) experiment of a RAZIB utilizing an α -MnO₂ cathode, with its corresponding voltage curve during cycles 2 to 4. (b) Gravimetric capacity and associated Mn dissolved percentage with respect to the initial mass in the electrode for the discharged and charged states of the RAZIB cell via *in situ* ¹H NMR.

that even a partially discharged phase (*e.g.*, α -Zn_{0.5}Mn₂O₄) is already electrochemically unstable due to the presence of unfavourably coordinated Zn²⁺ ions, causing the Mn dissolution to become energetically viable to occur. The ¹H NMR experiments also show that the

$[\text{Mn}_{(\text{aq})}^{2+}]$ in the electrolyte reduces upon charging of the RAZIB, as captured by the ^1H peak returns to lower chemical shifts throughout the charge process (see Fig. 5a). The reduction in $[\text{Mn}_{(\text{aq})}^{2+}]$ during charge is due to the electro-deposition of $\text{Mn}_{(\text{aq})}^{2+}$ ions on the electrode as $\text{MnO}_{2(\text{s})}$ [48, 50, 52], following the oxidative reaction of the $\text{Mn}_{(\text{aq})}^{2+}/\text{MnO}_{2(\text{s})}$ redox couple.

Finally, the gravimetric capacity and percentage of Mn dissolved from the electrode during the initial 20 cycles obtained from the *in situ* ^1H NMR experiments are shown in Fig. 5b. It is also possible to attest from these results that the Mn dissolution is reversible to a great extent, as the majority of the Mn atoms dissolved during discharge are determined to have electro-deposited on the electrode during cell charge. The electrochemically deposited phase has been shown to be comprised in its majority of MnO_2 , with Mn dissolution from the electrode occurring again in the following discharge cycle [48, 50, 52]. However, inactive phases, such as $\lambda\text{-ZnMn}_2\text{O}_4$, are also formed in the electrode during the electro-deposition process and do not dissolve into the electrolyte during the following discharge cycles [11, 24, 48, 51, 52]. The formation of a solid phase inactive to the proposed Mn dissolution mechanism will also cause a reduction in the obtained gravimetric capacity and $[\text{Mn}_{(\text{aq})}^{2+}]$ after each battery discharge, since a lower amount of Zn^{2+} ions will be able to intercalate into the electrode and assist the Mn dissolution. The reduction in gravimetric capacity and $[\text{Mn}_{(\text{aq})}^{2+}]$ after successive battery discharges can be clearly seen from the results shown in Fig. 5b. Also, from the data presented in Fig. 5b, it is possible to quantify the extent of the Mn dissolution to the electrolyte, with more than 40% of the Mn atoms initially in the $\alpha\text{-MnO}_2$ active material phase being demonstrated to dissolve into the electrolyte in the first discharge cycle.

The theoretical capacity for the $\alpha\text{-MnO}_2$ cathode considering only a Zn^{2+} intercalation mechanism is of 308 mA h g^{-1} . However, multiple studies have previously reported discharge capacities higher than the theoretical limit associated with Zn^{2+} intercalation in $\alpha\text{-MnO}_2$ cathodes for RAZIB [129, 130]. Exceeding the theoretical capacity should not be possible, unless there is an additional electrochemical reaction occurring alongside the Zn^{2+} intercalation that would be able to confer additional capacity. Differently from the JTE-assisted charge disproportionation reaction (Eqs. (1) and (2)), the unstable Zn coordination Mn dissolution mechanism proposed here is an electrochemical reaction (Eqs. (3) and (4)). Therefore, by considering an electrochemical Mn dissolution mechanism, both the Zn^{2+} intercalation and Mn dissolution would contribute to the battery capacity, allowing for ca-

pacities higher than the theoretical limit imposed by Zn^{2+} intercalation to be experimentally achieved. Overall, the Mn dissolution quantification results further showcase the considerable instability of RAZIB cells with α - MnO_2 cathodes, and highlight the urgency for viable strategies that can address the capacity fade for this material at practical cycling rates for grid-scale energy storage.

It is possible to conclude from the results presented in this study that the α - MnO_2 cathode for RAZIB is inherently unstable. First, capacity is gained through Zn^{2+} ion intercalation into α - MnO_2 during discharge to form a partially discharged α - $Zn_xMn_2O_4$ phase. The intercalated Zn^{2+} ions destabilize the electrode structure by establishing an energetically unfavourable bent coordination, which considerably lowers the energy required for Mn dissolution and consequently promotes the dissolution of $Mn^{2+}_{(aq)}$ into the electrolyte (i.e., the unstable Zn coordination Mn dissolution mechanism). During charging, the $Mn^{2+}_{(aq)}$ ions now present in the electrolyte at higher concentrations will then electro-deposit in the electrode forming electrochemically active (*e.g.*, MnO_2) and inactive (*e.g.*, $ZnMn_2O_4$) solid phases, with the latter negatively impacting the capacity gain in future cycles and ultimately causing the overall RAZIB capacity fade. Therefore, the Zn^{2+} intercalation process, which confers the Zn/α - MnO_2 battery its initial capacity during discharge, is also directly responsible for the battery capacity fade. The experimental 1H NMR results also showed that the Mn dissolution process occurs continuously during discharge, while the theoretical DFT results demonstrate that the dissolution can be energetically viable even for partially discharged materials. It is then possible to hypothesize that the Mn dissolution process in α - MnO_2 cathode occurs through the formation of an unstable layer of α - $Zn_xMn_2O_4$ on the material surface during the discharge, from which Mn atoms dissolve. As the dissolution occurs, a MnO_2 layer is expected to be established on the surface, with Zn^{2+} ions intercalating into the host structure and once again form the unstable α - $Zn_xMn_2O_4$ phase prone to Mn dissolution. A schematic for the proposed continuous Mn dissolution process occurring during RAZIB discharge in a representative α - MnO_2 particle is presented in Fig. 6.

It is then necessary to reduce the destabilizing effect that the Zn atoms have on the host structure in order to address the capacity fade issue found in α - MnO_2 cathodes for RAZIB. Two different strategies are proposed here: the inclusion of foreign elements in the tunnelled structure and the utilization of alloying/doping elements on the octahedral Mn site. Our results show that the unstable bent coordination established by the Zn atom after

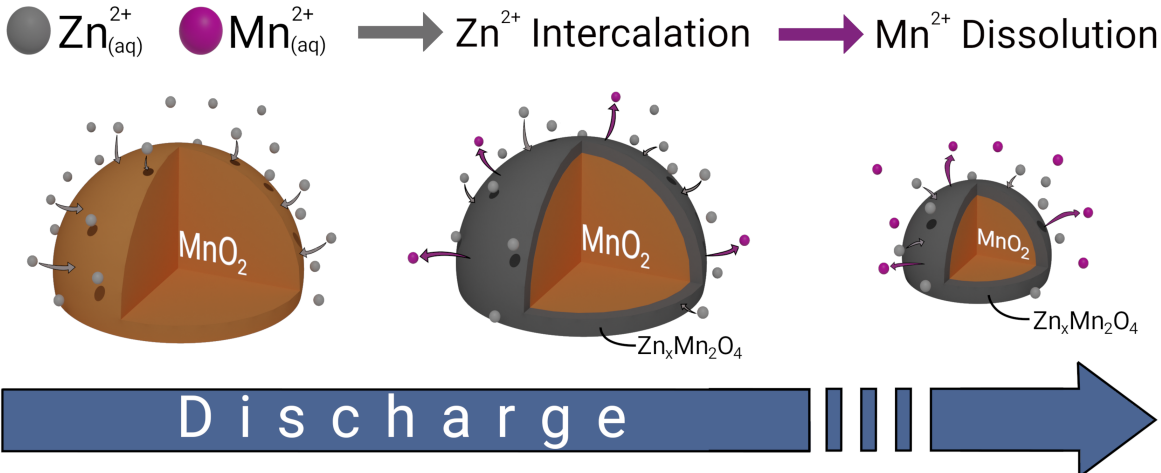


FIG. 6. Schematic for the Mn dissolution process occurring in α -MnO₂ particles during RAZIB discharge.

intercalation into the α -MnO₂ tunnel directly contributes to the low $E_d(V_{\text{Mn}}^q)$ calculated for α -ZnMn₂O₄. Therefore, the inclusion of a foreign atom into the tunnelled structure could potentially allow for a more stable coordination (*i.e.*, tetrahedral or octahedral) to be established for the intercalating Zn²⁺ ion, consequently increasing the associated $E_d(V_{\text{Mn}}^q)$. For example, chemical precursors containing light atoms, such as Li and Be, can be potentially added during synthesis of α -MnO₂ to support the stable intercalation of Zn²⁺ ions into the tunnelled structure, only adding a marginal increase in the molecular weight of the active material. It should be noted that the inclusion of a foreign element could potentially impact the intercalation/deintercalation process in structures with smaller tunnels (*e.g.*, α -MnO₂ - 2×2 tunnels) by reducing the available space for ionic diffusion inside the material. On the other hand, the capacity fade mitigation strategy of foreign element inclusion can be potentially more successful in MnO₂ polymorphs with wider tunnels (*e.g.*, Romanèchite-MnO₂ - 2×3 tunnels, Todorokite-MnO₂ - 3×3 tunnels), since a lower negative impact of foreign atom inclusion on the reversibility of the Zn²⁺ intercalation process would be expected. The chemical environment of the cathode material can also be modified with the incorporation of alloying/doping elements in place of Mn in the MnO₂ structure, contributing to an increase in the $E_d(V_{\text{Mn}}^q)$ after Zn²⁺ ions are intercalated. The alloying/doping atoms can potentially constrain the possibility of the Zn atoms to octahedrally coordinate at the V_{Mn} site after the vacancy is formed, which should considerably increase the calculated $E_d(V_{\text{Mn}}^q)$ in accordance to the ZnMn₂O₄ phases results. Even though the V_{Mn} formation will be invariably more en-

ergetically favourable in Zn-containing MnO_2 phases than in pristine MnO_2 (see discussion for Table I results), considerably higher $E_d(\text{V}_{\text{Mn}}^q)$ (*i.e.*, lower Mn dissolution feasibility) can still be achieved if Zn^{2+} is intercalated in a more favourable environment, as can be seen from the results of $\lambda\text{-ZnMn}_2\text{O}_4$. For example, oxides of Ti^{4+} and W^{6+} are electrochemically stable under RAZIB operation conditions [23], positioning them as ideal ions to be utilized in alloying/doping reactions to replace Mn atoms in MnO_2 cathodes.

CONCLUSIONS

Motivated by the previous uncertainty about the origin of the Mn dissolution during cycling of RAZIBs with MnO_2 cathodes, the formation of Mn vacancy (V_{Mn}) sites in completely charged ($\alpha\text{-MnO}_2$ and $\lambda\text{-MnO}_2$) and discharged ($\alpha\text{-ZnMn}_2\text{O}_4$ and $\lambda\text{-ZnMn}_2\text{O}_4$) Mn oxide phases was thoroughly investigated. The Mn dissolution was determined to be energetically favourable to occur on the discharged phase $\alpha\text{-ZnMn}_2\text{O}_4$ throughout the RAZIB potential window utilized for $\alpha\text{-MnO}_2$ electrode cycling. The Mn dissolution mechanism was concluded to result from the unstable bent coordination from the intercalating Zn^{2+} ions during discharge, prompting a substitution reaction to be energetically favourable, where a Mn atom dissolves into the electrolyte as $\text{Mn}_{(\text{aq})}^{2+}$ and a Zn atom octahedrally coordinates to the structure on the V_{Mn} site. The V_{Mn} formation energy for an $\alpha\text{-MnO}_2$ electrode during RAZIB cycling was then modelled, with the Mn dissolution shown to be energetically viable to occur even with low concentration of Zn^{2+} ions intercalated into the electrode ($x < 0.5$ in $\alpha\text{-Zn}_x\text{Mn}_2\text{O}_4$). The theoretical results were then corroborated by *operando* ^1H NMR experiments, which captured the continuous dissolution of Mn as $\text{Mn}_{(\text{aq})}^{2+}$ during discharge of a RAZIB cell with $\alpha\text{-MnO}_2$ cathode.

The unstable Zn coordination Mn dissolution mechanism proposed here for $\alpha\text{-MnO}_2$ cathodes in RAZIBs is also applicable for other cathodes materials and battery chemistries, since the unstable coordination of any intercalating ion into a cathode structure could promote the dissolution of the active material. Therefore, consideration for the intercalating ion coordination environment is shown here to be crucial during the investigation of cell degradation and proposal of novel cathode materials for ionic intercalation battery technologies. The discovery of the unstable Zn coordination Mn dissolution mechanism directly aid the development of novel strategies for capacity fade mitigation in RAZIB and other battery

chemistries, with two strategies concerning foreign atom inclusion on the structure and utilization of alloying/doping metals being proposed here. Overall, by uncovering origin of the Mn dissolution mechanism in α -MnO₂ cathodes during RAZIB cycling, a more comprehensive understanding of battery cathodes operation and degradation was achieved, directly supporting the design of stable battery technologies with prolonged operation lifetime.

ACKNOWLEDGMENTS

The authors gratefully acknowledge the financial support from [Salient Energy Inc.](#) and the [Natural Sciences and Engineering Research Council of Canada \(NSERC\)](#) Alliance Program. The SEM and nuclear magnetic resonance (NMR) experiments were respectively conducted at the [Canadian Centre for Electron Microscopy \(CCEM\)](#) and the [Nuclear Magnetic Resonance \(NMR\) Facility](#) at McMaster University, Canada. C.M.M. acknowledges the [Digital Research Alliance of Canada](#) and [Compute Ontario](#) for the computing resources utilized in this research.

Author Contributions:

- **Caio Miranda Miliante:** Conceptualization, Methodology (Theoretical), Validation, Formal analysis, Investigation (Theoretical), Data curation, Writing - Original Draft, Writing - Review & Editing, Visualization, and Project administration.
- **Kevin J. Sanders:** Methodology (Experimental), Investigation (Experimental) and Writing - Review & Editing.
- **Liam J. McGoldrick:** Investigation (Experimental) and Writing - Review & Editing.
- **Nicola Seriani:** Writing - Review & Editing.
- **Brian D. Adams:** Writing - Review & Editing, and Funding acquisition.
- **Gillian R. Goward:** Resources, Writing - Review & Editing, Supervision, and Funding acquisition.
- **Drew Higgins:** Resources, Writing - Review & Editing, Supervision, and Funding acquisition.

- **Oleg Rubel:** Conceptualization, Methodology, Resources, Writing - Review & Editing, Supervision, Funding acquisition.

Data Availability:

The data supporting this article is presented in the supplementary information (SI). The SI includes data for: SEM of α -MnO₂ particles; relaxed crystal structures of λ -MnO₂ and λ -ZnMn₂O₄; V_{Mn} site positions in and relaxed structures of α -MnO₂(V_{Mn}), λ -MnO₂(V_{Mn}), and λ -ZnMn₂O₄(V_{Mn}); schematic of the relationship between $E_d(V_{Mn}^0)$, $\Delta E_{rlx}(V_{Mn}^0)$, and $E_d(V_{Mn}^0)_{wor}$; structures of α -MnO₂(V_{Mn}), α -ZnMn₂O₄(V_{Mn1}), α -ZnMn₂O₄(V_{Mn2}), λ -MnO₂(V_{Mn}), and λ -ZnMn₂O₄(V_{Mn}) before and after atomic relaxation; $E_d(V_{Mn}^0)_{wor}$ results for Mn atoms in different oxidation states with respect to the chemical potential of Mn²⁺_(aq) in the RAZIB aqueous electrolyte; U_{local} results for α -MnO₂(V_{Mn}), λ -MnO₂(V_{Mn}) and λ -ZnMn₂O₄(V_{Mn}) structures before and after atomic relaxation; Mn vacancy formation energy ($E_d(V_{Mn}^q)$) as a function of the E_F for α -MnO₂(V_{Mn}), α -ZnMn₂O₄(V_{Mn1}), α -ZnMn₂O₄(V_{Mn2}), λ -MnO₂(V_{Mn}), and λ -ZnMn₂O₄(V_{Mn}).

Conflicts of Interest:

B.D.A. is co-founder and partial owner of Salient Energy Inc., which develops and commercializes rechargeable aqueous Zn-ion battery technology.

[1] A. Gallo, J. R. Simões-Moreira, H. Costa, M. M. Santos, and E. M. Dos Santos, Energy storage in the energy transition context: a technology review, *Renew. Sustain. Energy Rev.* **65**, 800 (2016).

[2] S. Sundararagavan and E. Baker, Evaluating energy storage technologies for wind power integration, *Sol. Energy* **86**, 2707 (2012).

[3] J. P. Barton and D. G. Infield, Energy storage and its use with intermittent renewable energy, *IEEE Trans. Energy Convers.* **19**, 441 (2004).

[4] M. Schoenfisch and A. Dasgupta, [Grid-scale storage](#) (2023), (acessed September 2024).

[5] S. W. Gourley, R. Brown, B. D. Adams, and D. Higgins, Zinc-ion batteries for stationary energy storage, *Joule* **7**, 1415 (2023).

[6] X. Luo, J. Wang, M. Dooner, and J. Clarke, Overview of current development in electrical

energy storage technologies and the application potential in power system operation, *Appl. Energy* **137**, 511 (2015).

[7] J. Arteaga, H. Zareipour, and V. Thangadurai, Overview of lithium-ion grid-scale energy storage systems, *Curr. Sustain./Renew. Energy Rep.* **4**, 197 (2017).

[8] B. Diouf and R. Pode, Potential of lithium-ion batteries in renewable energy, *Renew. Energy* **76**, 375 (2015).

[9] Y. Huang and J. Li, Key challenges for grid-scale lithium-ion battery energy storage, *Adv. Energy Mater.* **12**, 2202197 (2022).

[10] T. Hosaka, K. Kubota, A. S. Hameed, and S. Komaba, Research development on K-ion batteries, *Chem. Rev.* **120**, 6358 (2020).

[11] L. E. Blanc, D. Kundu, and L. F. Nazar, Scientific challenges for the implementation of Zn-ion batteries, *Joule* **4**, 771 (2020).

[12] Z. Pan, X. Liu, J. Yang, X. Li, Z. Liu, X. J. Loh, and J. Wang, Aqueous rechargeable multivalent metal-ion batteries: advances and challenges, *Adv. Energy Mater.* **11**, 2100608 (2021).

[13] G. Li, L. Sun, S. Zhang, C. Zhang, H. Jin, K. Davey, G. Liang, S. Liu, J. Mao, and Z. Guo, Developing cathode materials for aqueous zinc ion batteries: challenges and practical prospects, *Adv. Funct. Mater.* **34**, 2301291 (2024).

[14] T. Zhou, L. Zhu, L. Xie, Q. Han, X. Yang, L. Chen, G. Wang, and X. Cao, Cathode materials for aqueous zinc-ion batteries: a mini review, *J. Colloid Interface Sci.* **605**, 828 (2022).

[15] S. Huang, J. Zhu, J. Tian, and Z. Niu, Recent progress in the electrolytes of aqueous zinc-ion batteries, *Chem. Eur. J.* **25**, 14480 (2019).

[16] C. Li, S. Jin, L. A. Archer, and L. F. Nazar, Toward practical aqueous zinc-ion batteries for electrochemical energy storage, *Joule* **6**, 1733 (2022).

[17] H. Pan, Y. Shao, P. Yan, Y. Cheng, K. S. Han, Z. Nie, C. Wang, J. Yang, X. Li, P. Bhattacharya, *et al.*, Reversible aqueous zinc/manganese oxide energy storage from conversion reactions, *Nat. Energy* **1**, 16039 (2016).

[18] S. W. Gourley, C. Miranda Miliante, A. Ibarra-Espinoza, T. Baker, N. Noor, O. Rubel, B. D. Adams, and D. Higgins, The influence of nickel and alkali metal additives on manganese dioxide structure and performance for rechargeable zinc-ion batteries, *ACS Appl. Mater. Interfaces* **17**, 29558 (2025).

- [19] T. N. T. Tran, S. Jin, M. Cuisinier, B. D. Adams, and D. G. Ivey, Reaction mechanisms for electrolytic manganese dioxide in rechargeable aqueous zinc-ion batteries, *Sci. Rep.* **11**, 20777 (2021).
- [20] D. Kundu, B. D. Adams, V. Duffort, S. H. Vajargah, and L. F. Nazar, A high-capacity and long-life aqueous rechargeable zinc battery using a metal oxide intercalation cathode, *Nat. Energy* **1**, 4599 (2016).
- [21] W. Liu, J. Hao, C. Xu, J. Mou, L. Dong, F. Jiang, Z. Kang, J. Wu, B. Jiang, and F. Kang, Investigation of zinc ion storage of transition metal oxides, sulfides, and borides in zinc ion battery systems, *Chem. Commun.* **53**, 6872 (2017).
- [22] X. He, H. Zhang, X. Zhao, P. Zhang, M. Chen, Z. Zheng, Z. Han, T. Zhu, Y. Tong, and X. Lu, Stabilized molybdenum trioxide nanowires as novel ultrahigh-capacity cathode for rechargeable zinc ion battery, *Adv. Sci.* **6**, 1900151 (2019).
- [23] C. Miliante, S. Gourley, B. Adams, D. Higgins, and O. Rubel, Roadmap for the development of transition metal oxide cathodes for rechargeable zinc-ion batteries, *J. Phys. Chem. C* **128**, 17261 (2024).
- [24] O. Rubel, T. N. T. Tran, S. Gourley, S. Anand, A. V. Bommel, B. D. Adams, D. G. Ivey, and D. Higgins, Electrochemical stability of $ZnMn_2O_4$: understanding Zn-ion rechargeable battery capacity and degradation, *J. Phys. Chem. C* **126**, 10957 (2022).
- [25] R. Trócoli and F. La Mantia, An aqueous zinc-ion battery based on copper hexacyanoferrate, *ChemSusChem* **8**, 481 (2015).
- [26] Y. Zhang, Y. Wang, L. Lu, C. Sun, and Y. Denis, Vanadium hexacyanoferrate with two redox active sites as cathode material for aqueous Zn-ion batteries, *J. Power Sources* **484**, 229263 (2021).
- [27] Y. Cheng, L. Luo, L. Zhong, J. Chen, B. Li, W. Wang, S. X. Mao, C. Wang, V. L. Sprenkle, G. Li, *et al.*, Highly reversible zinc-ion intercalation into chevrel phase Mo_6S_8 nanocubes and applications for advanced zinc-ion batteries, *ACS Appl. Mater. Interfaces* **8**, 13673 (2016).
- [28] L. Wang, M. Jiang, F. Liu, Q. Huang, L. Liu, L. Fu, and Y. Wu, Layered TiS_2 as a promising host material for aqueous rechargeable Zn ion battery, *Energy Fuels* **34**, 11590 (2020).
- [29] L. Wang, S. Li, C. Wang, S. Yao, G. Chen, and F. Du, Recent advance and design strategies of chalcogenides for high-performance aqueous zinc-ion batteries, *J. Phys. D: Appl. Phys.* **57**, 253001 (2024).

[30] J. Li, L. Huang, H. Lv, J. Wang, G. Wang, L. Chen, Y. Liu, W. Guo, F. Yu, and T. Gu, Novel organic cathode with conjugated N-heteroaromatic structures for high-performance aqueous zinc-ion batteries, *ACS Appl. Mater. Interfaces* **14**, 38844 (2022).

[31] Y. Gao, G. Li, F. Wang, J. Chu, P. Yu, B. Wang, H. Zhan, and Z. Song, A high-performance aqueous rechargeable zinc battery based on organic cathode integrating quinone and pyrazine, *Energy Storage Mater.* **40**, 31 (2021).

[32] X. Geng, H. Ma, F. Lv, K. Yang, J. Ma, Y. Jiang, Q. Liu, D. Chen, Y. Jiang, and N. Zhu, Ultrastable organic cathode derived by pigment/rGO for aqueous zinc-ion batteries, *Chem. Eng. J.* **446**, 137289 (2022).

[33] A. I. Espinoza, T. J. Baker, S. W. Gourley, C. M. Miliante, K. J. Sanders, Z. Liu, G. R. Goward, O. Rubel, B. D. Adams, and D. Higgins, A tert-butyl functionalized quinone as active material for rechargeable aqueous zinc-ion batteries exhibiting high round-trip efficiency, *Future Batteries* **7**, 100092 (2025).

[34] T. J. Baker, A. I. Espinoza, S. W. Gourley, B. D. Adams, and D. Higgins, Stabilizing redox-active organic molecules via grafting to carbon for cathodes in aqueous rechargeable zinc-ion batteries, *J. Energy Storage* **150**, 120312 (2026).

[35] A. W. Frazier, W. Cole, P. Denholm, S. Machen, N. Gates, and N. Blair, *Storage futures study: economic potential of diurnal storage in the US power sector*, National Renewable Energy Lab (NREL) (2021).

[36] G. Zampardi and F. La Mantia, Prussian blue analogues as aqueous Zn-ion batteries electrodes: Current challenges and future perspectives, *Curr. Opin. Electrochem.* **21**, 84 (2020).

[37] H. Cui, L. Ma, Z. Huang, Z. Chen, and C. Zhi, Organic materials-based cathode for zinc ion battery, *SmartMat* **3**, 565 (2022).

[38] D. Selvakumaran, A. Pan, S. Liang, and G. Cao, A review on recent developments and challenges of cathode materials for rechargeable aqueous Zn-ion batteries, *J. Mater. Chem. A* **7**, 18209 (2019).

[39] T. Xue and H. J. Fan, From aqueous Zn-ion battery to Zn-MnO₂ flow battery: A brief story, *J. Energy Chem.* **54**, 194 (2021).

[40] T. Yamamoto and T. Shoji, Rechargeable Zn|ZnSO₄|MnO₂-type cells, *Inorg. Chim. Acta* **117**, L27 (1986).

[41] Z. Azmi, K. C. Senapati, A. K. Goswami, and S. R. Mohapatra, A comprehensive review

of strategies to augment the performance of MnO_2 cathode by structural modifications for aqueous zinc ion battery, *J. Power Sources* **613**, 234816 (2024).

- [42] H. Tang, W. Chen, N. Li, Z. Hu, L. Xiao, Y. Xie, L. Xi, L. Ni, and Y. Zhu, Layered MnO_2 nanodots as high-rate and stable cathode materials for aqueous zinc-ion storage, *Energy Storage Mater.* **48**, 335 (2022).
- [43] J. Wang, J.-G. Wang, H. Liu, Z. You, Z. Li, F. Kang, and B. Wei, A highly flexible and lightweight MnO_2 /graphene membrane for superior zinc-ion batteries, *Adv. Funct. Mater.* **31**, 2007397 (2021).
- [44] J. Li, X. Yang, D. Ma, J. Liu, C. Ma, N. Liu, L. Lu, T. Wang, X. Pang, Y. Yang, *et al.*, Multi-layered carbon accommodation of MnO_2 enabling fast kinetics for highly stable zinc ion batteries, *J. Colloid Interface Sci.* **676**, 927 (2024).
- [45] X. Xu, Y. Chen, W. Li, R. Yin, D. Zheng, X. Niu, X. Dai, W. Shi, W. Liu, F. Wu, *et al.*, Achieving ultralong-cycle zinc-ion battery via synergistically electronic and structural regulation of a MnO_2 nanocrystal–carbon hybrid framework, *Small* **19**, 2207517 (2023).
- [46] H. Wang, M. Liang, J. Gao, C. Ma, Z. He, Y. Zhao, and Z. Miao, Robust structural stability of flower-like $\delta\text{-MnO}_2$ as cathode for aqueous zinc ion battery, *Colloids Surf. A: Physicochem. Eng. Asp.* **643**, 128804 (2022).
- [47] Y. Wang, L. Liu, Y. Wang, J. Qu, Y. Chen, and J. Song, Atomically coupled 2D MnO_2 /MXene superlattices for ultrastable and fast aqueous zinc-ion batteries, *ACS Nano* **17**, 21761 (2023).
- [48] B. Lee, C. S. Yoon, H. R. Lee, K. Y. Chung, B. W. Cho, and S. H. Oh, Electrochemically-induced reversible transition from the tunneled to layered polymorphs of manganese dioxide, *Sci. Rep.* **4**, 6066 (2014).
- [49] M. H. Alfaruqi, S. Islam, D. Y. Putro, V. Mathew, S. Kim, J. Jo, S. Kim, Y.-K. Sun, K. Kim, and J. Kim, Structural transformation and electrochemical study of layered MnO_2 in rechargeable aqueous zinc-ion battery, *Electrochim. Acta* **276**, 1 (2018).
- [50] D. Wu, L. M. Housel, S. J. Kim, N. Sadique, C. D. Quilty, L. Wu, R. Tappero, S. L. Nicholas, S. Ehrlich, Y. Zhu, *et al.*, Quantitative temporally and spatially resolved X-ray fluorescence microprobe characterization of the manganese dissolution-deposition mechanism in aqueous $\text{Zn}/\alpha\text{-MnO}_2$ batteries, *Energy Environ. Sci.* **13**, 4322 (2020).
- [51] N. Zhang, J. Wang, X. Liu, P.-F. Wang, Y.-G. Liu, Y. Xie, and T.-F. Yi, Towards high-

performance aqueous Zn–MnO₂ batteries: Formation mechanism and alleviation strategies of irreversible inert phases, *Compos. B: Eng.* **260**, 110770 (2023).

- [52] Y. Liao, H.-C. Chen, C. Yang, R. Liu, Z. Peng, H. Cao, and K. Wang, Unveiling performance evolution mechanisms of MnO₂ polymorphs for durable aqueous zinc-ion batteries, *Energy Storage Mater.* **44**, 508 (2022).
- [53] U. Siamionau, Y. Aniskevich, A. Mazanik, O. Kokits, G. Ragoisha, J. H. Jo, S.-T. Myung, and E. Streltsov, Rechargeable zinc-ion batteries with manganese dioxide cathode: How critical is choice of manganese dioxide polymorphs in aqueous solutions?, *J. Power Sources* **523**, 231023 (2022).
- [54] Y. Cai, R. Chua, S. Huang, H. Ren, and M. Srinivasan, Amorphous manganese dioxide with the enhanced pseudocapacitive performance for aqueous rechargeable zinc-ion battery, *Chem. Eng. J.* **396**, 125221 (2020).
- [55] N. Zhang, F. Cheng, J. Liu, L. Wang, X. Long, X. Liu, F. Li, and J. Chen, Rechargeable aqueous zinc-manganese dioxide batteries with high energy and power densities, *Nat. Commun.* **8**, 1 (2017).
- [56] J. Heo, S. Chong, S. Kim, R. Kim, K. Shin, J. Kim, and H.-T. Kim, Suppressing charge disproportionation of MnO₂ cathodes in rechargeable zinc ion batteries via cooperative Jahn–Teller distortion, *Batter. Supercaps* **4**, 1881 (2021).
- [57] X. Li, Y. Sun, L. Zhou, H. Wang, B. Xie, W. Lu, J. Ning, and Y. Hu, Suppressing Jahn–Teller distortion and locking lattice water with doped Fe(III) in birnessite toward fast and stable zinc-ion batteries, *Mater. Horiz.* **11**, 4133 (2024).
- [58] M. M. Thackeray, Y. Shao-Horn, A. J. Kahaian, K. D. Kepler, E. Skinner, J. T. Vaughey, and S. A. Hackney, Structural fatigue in spinel electrodes in high voltage (4 V) Li/Li_xMn₂O₄ cells, *Electrochem. Solid-State Lett.* **1**, 7 (1998).
- [59] R. Gummow, A. De Kock, and M. Thackeray, Improved capacity retention in rechargeable 4 V lithium/lithium-manganese oxide (spinel) cells, *Solid State Ion.* **69**, 59 (1994).
- [60] M. M. Thackeray, Manganese oxides for lithium batteries, *Prog. Solid State Chem.* **25**, 1 (1997).
- [61] M. Thackeray, P. Johnson, L. De Picciotto, P. Bruce, and J. Goodenough, Electrochemical extraction of lithium from LiMn₂O₄, *Mater. Res. Bull.* **19**, 179 (1984).
- [62] H. Berg, K. Göransson, B. Noläng, and J. O. Thomas, Electronic structure and stability of

the $\text{Li}_x\text{Mn}_2\text{O}_4$ ($1 < x < 2$) system, *J. Mater. Chem.* **9**, 2813 (1999).

[63] L.-F. Wang, C.-C. Ou, K. A. Striebel, and J.-S. Chen, Study of Mn dissolution from LiMn_2O_4 spinel electrodes using rotating ring-disk collection experiments, *J. Electrochem. Soc.* **150**, A905 (2003).

[64] A. Bhandari and J. Bhattacharya, Manganese dissolution from spinel cathode: few unanswered questions, *J. Electrochem. Soc.* **164**, A106 (2016).

[65] D. H. Jang, Y. J. Shin, and S. M. Oh, Dissolution of spinel oxides and capacity losses in 4 v $\text{Li}/\text{Li}_x\text{Mn}_2\text{O}_4$ cells, *J. Electrochem. Soc.* **143**, 2204 (1996).

[66] K. Takahashi, M. Saitoh, N. Asakura, T. Hibino, M. Sano, M. Fujita, and K. Kifune, Electrochemical properties of lithium manganese oxides with different surface areas for lithium ion batteries, *J. Power Sources* **136**, 115 (2004).

[67] H. Shiiba, N. Zettsu, M. Nakayama, S. Oishi, and K. Teshima, Defect formation energy in spinel $\text{LiNi}_{0.5}\text{Mn}_{1.5}\text{O}_{4-\delta}$ using ab initio DFT calculations, *J. Phys. Chem. C* **119**, 9117 (2015).

[68] B. Ammundsen, J. Rozière, and M. S. Islam, Atomistic simulation studies of lithium and proton insertion in spinel lithium manganates, *J. Phys. Chem. B* **101**, 8156 (1997).

[69] J. Zhou, G. Chen, K. Wu, Y. Cheng, B. Peng, J. Guo, and Y. Jiang, Density functional theory study on oxygen adsorption in LaSrCoO_4 : An extended cathode material for solid oxide fuel cells, *Appl. Surf. Sci.* **258**, 3133 (2012).

[70] W. Ma, B. Zhou, J. Wang, X. Zhang, and Z. Jiang, Effect of oxygen vacancy on Li-ion diffusion in a V_2O_5 cathode: a first-principles study, *J. Phys. D: Appl. Phys.* **46**, 105306 (2013).

[71] W. Hu, H. Wang, W. Luo, B. Xu, and C. Ouyang, Formation and thermodynamic stability of oxygen vacancies in typical cathode materials for Li-ion batteries: Density functional theory study, *Solid State Ion.* **347**, 115257 (2020).

[72] K. Leung, First-principles modeling of Mn(II) migration above and dissolution from $\text{Li}_x\text{Mn}_2\text{O}_4$ (001) surfaces, *Chem. Mater.* **29**, 2550 (2017).

[73] A. Abbaspour-Tamijani, J. W. Bennett, D. T. Jones, N. Cartagena-Gonzalez, Z. R. Jones, E. D. Laudadio, R. J. Hamers, J. A. Santana, and S. E. Mason, DFT and thermodynamics calculations of surface cation release in LiCoO_2 , *Appl. Surf. Sci.* **515**, 145865 (2020).

[74] X. Huang, J. W. Bennett, M. N. Hang, E. D. Laudadio, R. J. Hamers, and S. E. Mason, Ab initio atomistic thermodynamics study of the (001) surface of LiCoO_2 in a water environment

and implications for reactivity under ambient conditions, *J. Phys. Chem. C* **121**, 5069 (2017).

[75] J. W. Bennett, D. Jones, X. Huang, R. J. Hamers, and S. E. Mason, Dissolution of complex metal oxides from first-principles and thermodynamics: Cation removal from the (001) surface of $\text{Li}(\text{Ni}_{1/3}\text{Mn}_{1/3}\text{Co}_{1/3})\text{O}_2$, *Environ. Sci. Technol.* **52**, 5792 (2018).

[76] B. G. Hudson, D. T. Jones, V. M. Rivera Bustillo, J. W. Bennett, and S. E. Mason, Understanding the mechanism of secondary cation release from the (001) surface of $\text{Li}(\text{Ni}_{1/3}\text{Mn}_{1/3}\text{Co}_{1/3})\text{O}_2$: Insights from first-principles, *J. Phys. Chem. C* **127**, 21022 (2023).

[77] C. Cai, D. Zhang, Q. Zhang, K. Chen, W. Hua, C. Peng, and D. Xue, Origin of oxygen-redox and transition metals dissolution in Ni-rich $\text{Li}_x\text{Ni}_{0.8}\text{Co}_{0.1}\text{Mn}_{0.1}\text{O}_2$ cathode, *J. Chem. Phys.* **158**, 114703 (2023).

[78] Y. He, H. Pham, Y. Gao, R. L. Patel, S. Sarkar, X. Liang, and J. Park, Discovery of an unexpected metal dissolution of thin-coated cathode particles and its theoretical explanation, *Adv. Theory Simul.* **3**, 2000002 (2020).

[79] J. P. Perdew, K. Burke, and M. Ernzerhof, Generalized gradient approximation made simple, *Phys. Rev. Lett.* **77**, 3865 (1996).

[80] G. Kresse and J. Hafner, Ab initio molecular dynamics for liquid metals, *Phys. Rev. B* **47**, 558 (1993).

[81] G. Kresse and J. Furthmüller, Efficiency of ab-initio total energy calculations for metals and semiconductors using a plane-wave basis set, *Comp. Mater. Sci.* **6**, 15 (1996).

[82] G. Kresse and J. Furthmüller, Efficient iterative schemes for ab initio total-energy calculations using a plane-wave basis set, *Phys. Rev. B* **54**, 11169 (1996).

[83] G. Kresse and D. Joubert, From ultrasoft pseudopotentials to the projector augmented-wave method, *Phys. Rev. B* **59**, 1758 (1999).

[84] S. Grimme, J. Antony, S. Ehrlich, and H. Krieg, A consistent and accurate ab initio parametrization of density functional dispersion correction (DFT-D) for the 94 elements H-Pu, *J. Chem. Phys.* **132**, 154104 (2010).

[85] S. Grimme, S. Ehrlich, and L. Goerigk, Effect of the damping function in dispersion corrected density functional theory, *J. Comput. Chem.* **32**, 1456 (2011).

[86] A. D. Becke and E. R. Johnson, A density-functional model of the dispersion interaction, *J. Chem. Phys.* **123**, 154101 (2005).

[87] E. R. Johnson and A. D. Becke, A post-hartree–fock model of intermolecular interactions, *J.*

Chem. Phys. **123**, 024101 (2005).

[88] E. R. Johnson and A. D. Becke, A post-hartree-fock model of intermolecular interactions: Inclusion of higher-order corrections, J. Chem. Phys. **124**, 174104 (2006).

[89] S. L. Dudarev, G. A. Botton, S. Y. Savrasov, C. J. Humphreys, and A. P. Sutton, Electron-energy-loss spectra and the structural stability of nickel oxide: An LSDA+U study, Phys. Rev. B **57**, 1505 (1998).

[90] A. Jain, G. Hautier, S. P. Ong, C. J. Moore, C. C. Fischer, K. A. Persson, and G. Ceder, Formation enthalpies by mixing GGA and GGA + *U* calculations, Phys. Rev. B **84**, 045115 (2011).

[91] Y. Crespo and N. Seriani, Electronic and magnetic properties of α -MnO₂ from ab initio calculations, Phys. Rev. B **88**, 144428 (2013).

[92] B. Wu, G. Zhang, M. Yan, T. Xiong, P. He, L. He, X. Xu, and L. Mai, Graphene scroll-coated α -MnO₂ nanowires as high-performance cathode materials for aqueous Zn-ion battery, Small **14**, 1703850 (2018).

[93] N. Zhang, Y.-R. Ji, J.-C. Wang, P.-F. Wang, Y.-R. Zhu, and T.-F. Yi, Understanding of the charge storage mechanism of MnO₂-based aqueous zinc-ion batteries: Reaction processes and regulation strategies, J. Energy Chem. **82**, 423 (2023).

[94] P. Patra, I. Naik, H. Bhatt, and S. Kaushik, Structural, infrared spectroscopy and magnetic properties of spinel ZnMn₂O₄, Physica B **572**, 199 (2019).

[95] L. S. Lobo and A. Ruban Kumar, Investigation of structural and electrical properties of ZnMn₂O₄ synthesized by sol-gel method, J. Mater. Sci. **27**, 7398 (2016).

[96] F. M. Courtel, Y. Abu-Lebdeh, and I. J. Davidson, ZnMn₂O₄ nanoparticles synthesized by a hydrothermal method as an anode material for Li-ion batteries, Electrochim. Acta **71**, 123 (2012).

[97] A. Jain, S. P. Ong, G. Hautier, W. Chen, W. D. Richards, S. Dacek, S. Cholia, D. Gunter, D. Skinner, G. Ceder, *et al.*, Commentary: The Materials Project: A materials genome approach to accelerating materials innovation, APL Mater. **1**, 011002 (2013).

[98] N. Kijima, T. Ikeda, K. Oikawa, F. Izumi, and Y. Yoshimura, Crystal structure of an open-tunnel oxide α -MnO₂ analyzed by rietveld refinements and mem-based pattern fitting, J. Solid State Chem. **177**, 1258 (2004).

[99] J. C. Hunter, Preparation of a new crystal form of manganese dioxide: λ -MnO₂, J. Solid

State Chem. **39**, 142 (1981).

- [100] Menaka, M. Qamar, S. E. Lofland, K. V. Ramanujachary, and A. K. Ganguli, Magnetic and photocatalytic properties of nanocrystalline $ZnMn_2O_4$, Bull. Mater. Sci. **32**, 231 (2009).
- [101] S. Zhang and J. Northrup, Chemical potential dependence of defect formation energies in GaAs: application to Ga self-diffusion, Phys. Rev. Lett. **67**, 2339 (1991).
- [102] C. Freysoldt, B. Grabowski, T. Hickel, J. Neugebauer, G. Kresse, A. Janotti, and C. G. Van de Walle, First-principles calculations for point defects in solids, Rev. Mod. Phys. **86**, 253 (2014).
- [103] O. Rubel and X. Rocquefelte, Defect tolerance of lead-halide perovskite (100) surface relative to bulk: band bending, surface states, and characteristics of vacancies, J. Phys. Chem. C **128**, 5667 (2024).
- [104] X. Rong and A. M. Kolpak, Ab initio approach for prediction of oxide surface structure, stoichiometry, and electrocatalytic activity in aqueous solution, J. Phys. Chem. Lett. **6**, 1785 (2015).
- [105] S. Lany and A. Zunger, Accurate prediction of defect properties in density functional supercell calculations, Model. Simul. Mater. Sci. Eng. **17**, 084002 (2009).
- [106] C. Freysoldt, J. Neugebauer, and C. G. Van de Walle, Fully *ab initio* finite-size corrections for charged-defect supercell calculations, Phys. Rev. Lett. **102**, 016402 (2009).
- [107] D. Hobbs, J. Hafner, and D. Spišák, Understanding the complex metallic element Mn. i. crystalline and noncollinear magnetic structure of α -Mn, Phys. Rev. B **68**, 014407 (2003).
- [108] M. Pourbaix, *Atlas of electrochemical equilibria in aqueous solutions*, 2nd ed. (National Association of Corrosion Engineers, 1974) pp. 286–293.
- [109] M. Chamoun, W. R. Brant, C.-W. Tai, G. Karlsson, and D. Noréus, Rechargeability of aqueous sulfate Zn/MnO_2 batteries enhanced by accessible Mn^{2+} ions, Energy Stor. Mater. **15**, 351 (2018).
- [110] S. Cui, D. Zhang, and Y. Gan, The effect of Mn^{2+} additives on the capacity of aqueous $Zn/\delta\text{--}MnO_2$ batteries: Elucidating the Mn^{2+} concentration dependence of the irreversible transformation of $\delta\text{--}MnO_2$, J. Power Sources **579**, 233293 (2023).
- [111] J. Rumble, *CRC Handbook of Chemistry and Physics* (CRC Press, 2023) pp. 9–97–9–103.
- [112] C. Liu, X. Xie, B. Lu, J. Zhou, and S. Liang, Electrolyte strategies toward better zinc-ion batteries, ACS Energy Lett. **6**, 1015 (2021).

[113] O. Rubel, <https://github.com/rubel75/PyDEF-2.0> (2023), accessed: 2024-11-01.

[114] A. Stoliaroff, S. Jobic, and C. Latouche, PyDEF 2.0: an easy to use post-treatment software for publishable charts featuring a graphical user interface, *J. Comput. Chem.* **39**, 2251 (2018).

[115] E. Péan, J. Vidal, S. Jobic, and C. Latouche, Presentation of the PyDEF post-treatment Python software to compute publishable charts for defect energy formation, *Chem. Phys. Lett.* **671**, 124 (2017).

[116] M. H. Naik and M. Jain, CoFFEE: corrections for formation energy and eigenvalues for charged defect simulations, *Comput. Phys. Commun.* **226**, 114 (2018).

[117] K. J. Sanders, A. R. Aguilera, J. R. Keffer, B. J. Balcom, I. C. Halalay, and G. R. Goward, Transient lithium metal plating on graphite: *Operando* ^7Li nuclear magnetic resonance investigation of a battery cell using a novel RF probe, *Carbon* **189**, 377 (2022).

[118] K. J. Sanders, A. A. Ciezki, A. Berno, I. C. Halalay, and G. R. Goward, Quantitative *operando* ^7Li NMR investigations of silicon anode evolution during fast charging and extended cycling, *J. Am. Chem. Soc* **145**, 21502 (2023).

[119] A. R. Aguilera, K. J. Sanders, G. R. Goward, and B. J. Balcom, The parallel-plate resonator: an RF probe for MR and MRI studies over a wide frequency range, *Magn. Reson. Lett.* **3**, 306 (2023).

[120] K. J. Sanders, B. L. Pinto, A. Cheng, L. J. McGoldrick, Z. Liu, R. Jadhav, S. W. Gourley, A. Ibarra-Espinoza, C. M. Miliante, W. Tran, B. D. Adams, O. Rubel, D. Higgins, and G. R. Goward, Reversible Mn^{2+} dissolution-deposition in Zn- MnO_2 cells revealed by ^1H NMR spectroscopy, Submitted (*Under Review*) (2026).

[121] Z. Sadighi, K. Sanders, E. Magee, A. Quadiri, J. Gao, I. Yoon, B. Koch, and G. Goward, Quantitative investigation of lithium metal plating via *operando* ^7Li NMR spectroscopy of a unique three electrode lithium-ion battery, *ChemRxiv* [10.26434/chemrxiv-2025-1jxxk](https://doi.org/10.26434/chemrxiv-2025-1jxxk) (2025).

[122] M. J. Young, A. M. Holder, S. M. George, and C. B. Musgrave, Charge storage in cation incorporated $\alpha\text{-MnO}_2$, *Chem. Mater.* **27**, 1172 (2015).

[123] L. Song, Y. Duan, Y. Zhang, and T. Wang, Promoting defect formation and microwave loss properties in $\delta\text{-MnO}_2$ via Co doping: a first-principles study, *Comput. Mater. Sci.* **138**, 288 (2017).

[124] P. Barak and P. A. Helmke, The chemistry of zinc, in *Zinc in Soils and Plants: Proceedings of the International Symposium on 'Zinc in Soils and Plants' held at The University of Western*

Australia, 27–28 September, 1993, edited by A. D. Robson (Springer Netherlands, Dordrecht, 1993) pp. 1–13.

- [125] H. Neumann, Notes on the mineralogy and geochemistry of zinc, *Mineral. Mag. J. Mineral. Soc.* **28**, 575 (1949).
- [126] B. Brehler, *Elements Cr (24) to Br (35): Zinc - Crystal Chemistry*, edited by K. H. Wedepohl, C. W. Correns, D. M. Shaw, K. K. Turekian, and J. Zemann, *Handbook of Geochemistry*:II-3, Vol. 1 (Springer, 1969) Chap. 30-A.
- [127] Y. Jean, *Molecular orbitals of transition metal complexes* (OUP Oxford, 2005) Chap. 2.
- [128] C. Deng, X. Li, R. Chen, K. Ye, J. Lipton, S. A. Maclean, H. Wang, A. D. Taylor, and G. Weng, Recent advances in rocking chair batteries and beyond, *Energy Storage Mater.* **60**, 102820 (2023).
- [129] W. Sun, F. Wang, S. Hou, C. Yang, X. Fan, Z. Ma, T. Gao, F. Han, R. Hu, M. Zhu, and C. Wang, Zn/MnO₂ battery chemistry with H⁺ and Zn²⁺ coininsertion, *J. Am. Chem. Soc.* **139**, 9775 (2017).
- [130] W. Shi, W. S. V. Lee, and J. Xue, Recent development of Mn-based oxides as zinc-ion battery cathode, *ChemSusChem* **14**, 1634 (2021).

Supplemental Material - Unveiling the origin of the capacity fade in MnO_2 zinc-ion battery cathodes through an analysis of the Mn vacancy formation

Caio Miranda Miliante,^{1,*} Kevin J. Sanders,² Liam J. McGoldrick,² Nicola Seriani,³ Brian D. Adams,⁴ Gillian R. Goward,² Drew Higgins,⁵ and Oleg Rubel¹

¹*Department of Materials Science and Engineering,
McMaster University, 1280 Main Street West,
Hamilton, Ontario L8S 4L8, Canada*

²*Department of Chemistry & Chemical Biology,
McMaster University, 1280 Main Street West,
Hamilton, Ontario L8S 4L8, Canada*

³*Condensed Matter and Statistical Physics Section,
The Abdus Salam ICTP, Strada Costiera 11, 34151 Trieste, Italy*

⁴*Salient Energy Inc., 21 McCurdy Avenue,
Dartmouth, Nova Scotia B3B 1C4, Canada*

⁵*Department of Chemical Engineering,
McMaster University, 1280 Main Street West,
Hamilton, Ontario L8S 4L8, Canada*

(Dated: February 16, 2026)

* miliante@mcmaster.ca

TABLE S1. Comparison between the experimental and the relaxed supercell crystallographic parameters for α -MnO₂, λ -MnO₂, and λ -ZnMn₂O₄. The parameters reported for the supercells are calculated by dividing the relaxed supercell parameters by the respective number of cell replications utilized when creating the supercell. All materials are from tetragonal or cubic space groups, thus having all lattice angles (α , β , and γ) equal to 90°.

Material	Space Group	Phase	a	b	c
α -MnO ₂	I4/m	Supercell (2x2x3)	9.640	9.640	2.888
		Exp. [98]	9.814	9.814	2.850
λ -MnO ₂	Fd $\bar{3}$ m	Supercell (2x2x2)	8.008	8.008	8.008
		Exp. [99]	8.03	8.03	8.03
λ -ZnMn ₂ O ₄	I4 ₁ /amd	Supercell (2x2x1)	5.737	5.737	9.139
		Exp. [100]	5.709	5.709	9.238

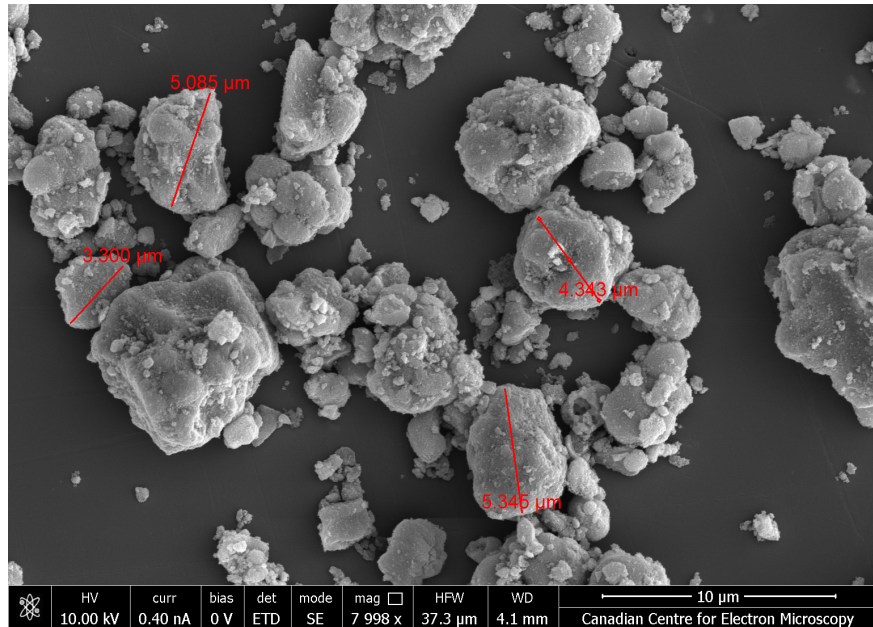


FIG. S1. Scanning electron microscopy (SEM) image of α -MnO₂ active material utilized in experimental testings.

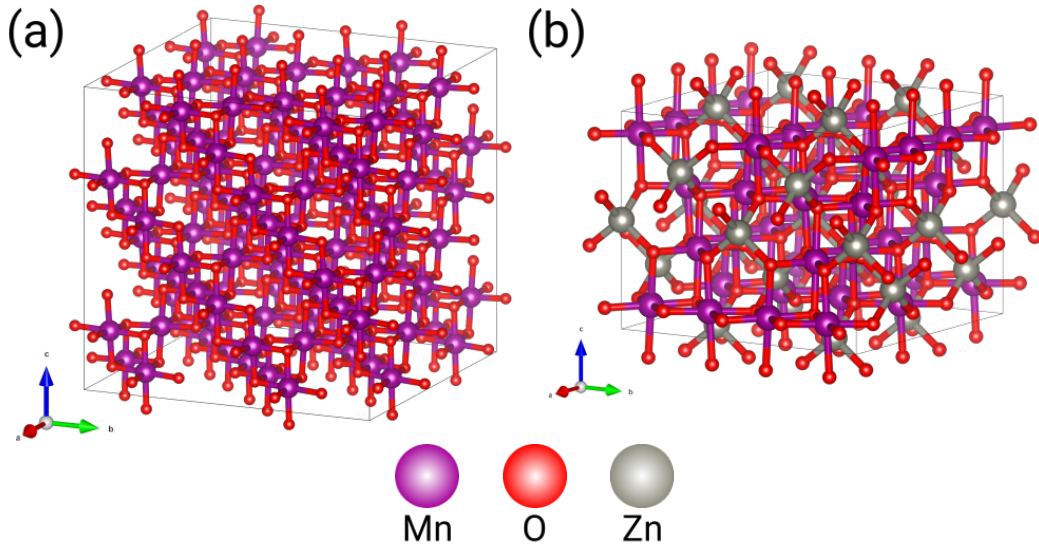


FIG. S2. Relaxed crystal structures of bulk (a) λ -MnO₂ and (b) λ -ZnMn₂O₄.

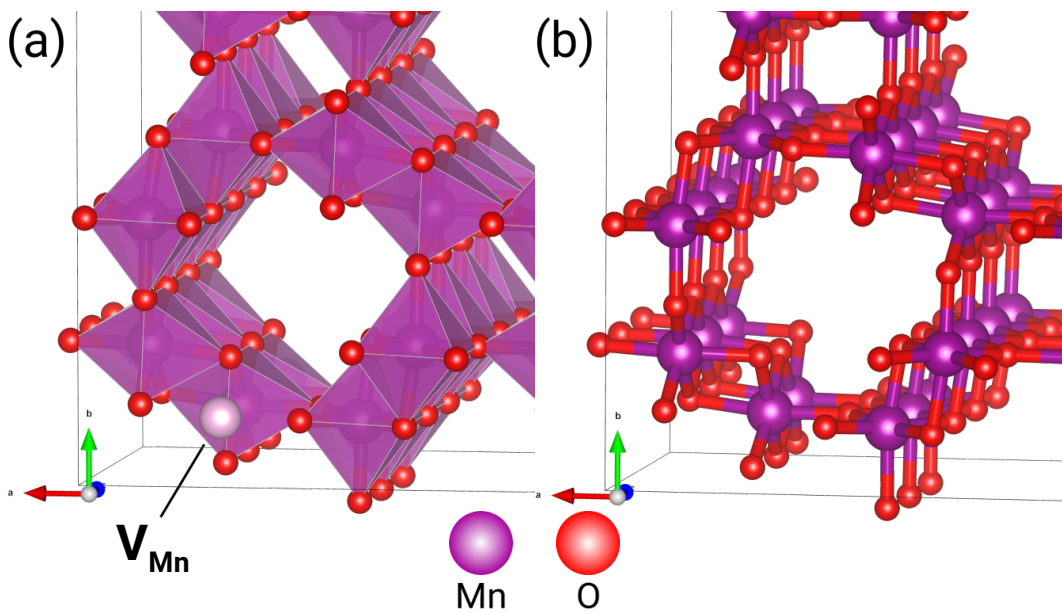


FIG. S3. (a) V_{Mn} site in the α -MnO₂ crystal structure indicated by lighter shaded Mn atom. (b) Relaxed structure of α -MnO₂(V_{Mn}) for a neutral charge defect. Only a zoomed in region of the simulated α -MnO₂(V_{Mn}) cells is shown to facilitate the visual analysis of the V_{Mn} positioning.

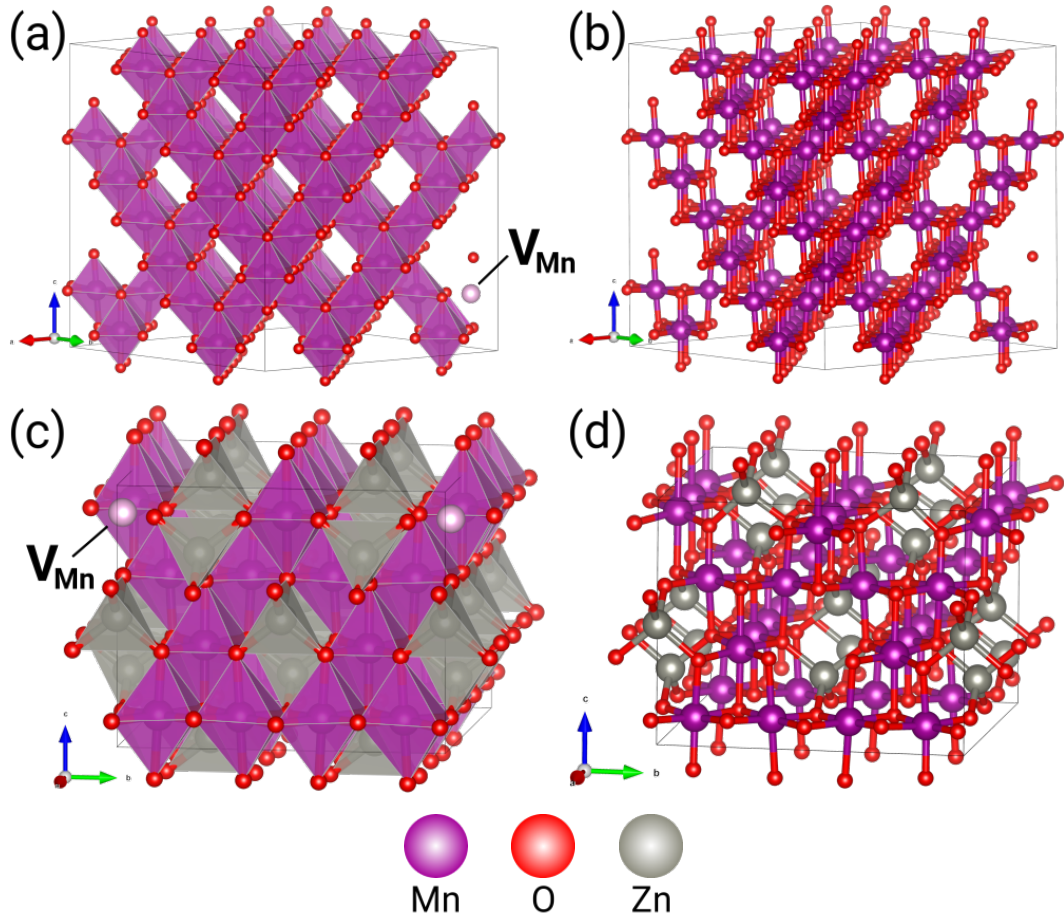


FIG. S4. V_{Mn} sites in the (a) λ -MnO₂ and (c) λ -ZnMn₂O₄ crystal structures indicated by lighter shaded Mn atoms. Relaxed structures of (b) λ -MnO₂(V_{Mn}) and (d) λ -ZnMn₂O₄(V_{Mn}) for a neutral charge defect.

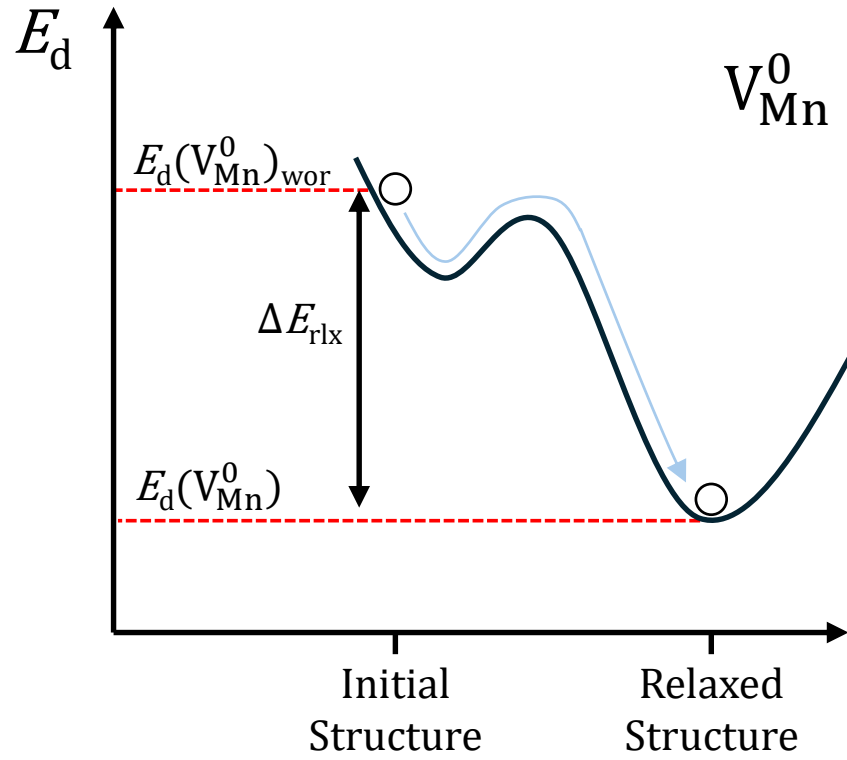


FIG. S5. Configuration energy diagram depicting the relationship between the neutral Mn vacancy formation energy ($E_d(V_{\text{Mn}}^0)$), the cell relaxation energy variation for neutral Mn vacancy ($\Delta E_{\text{rlx}}(V_{\text{Mn}}^0)$), and the neutral Mn vacancy formation energy without relaxation ($E_d(V_{\text{Mn}}^0)_{\text{wor}}$) with respect to the energy profile of a structure containing a neutral Mn vacancy (V_{Mn}^0).

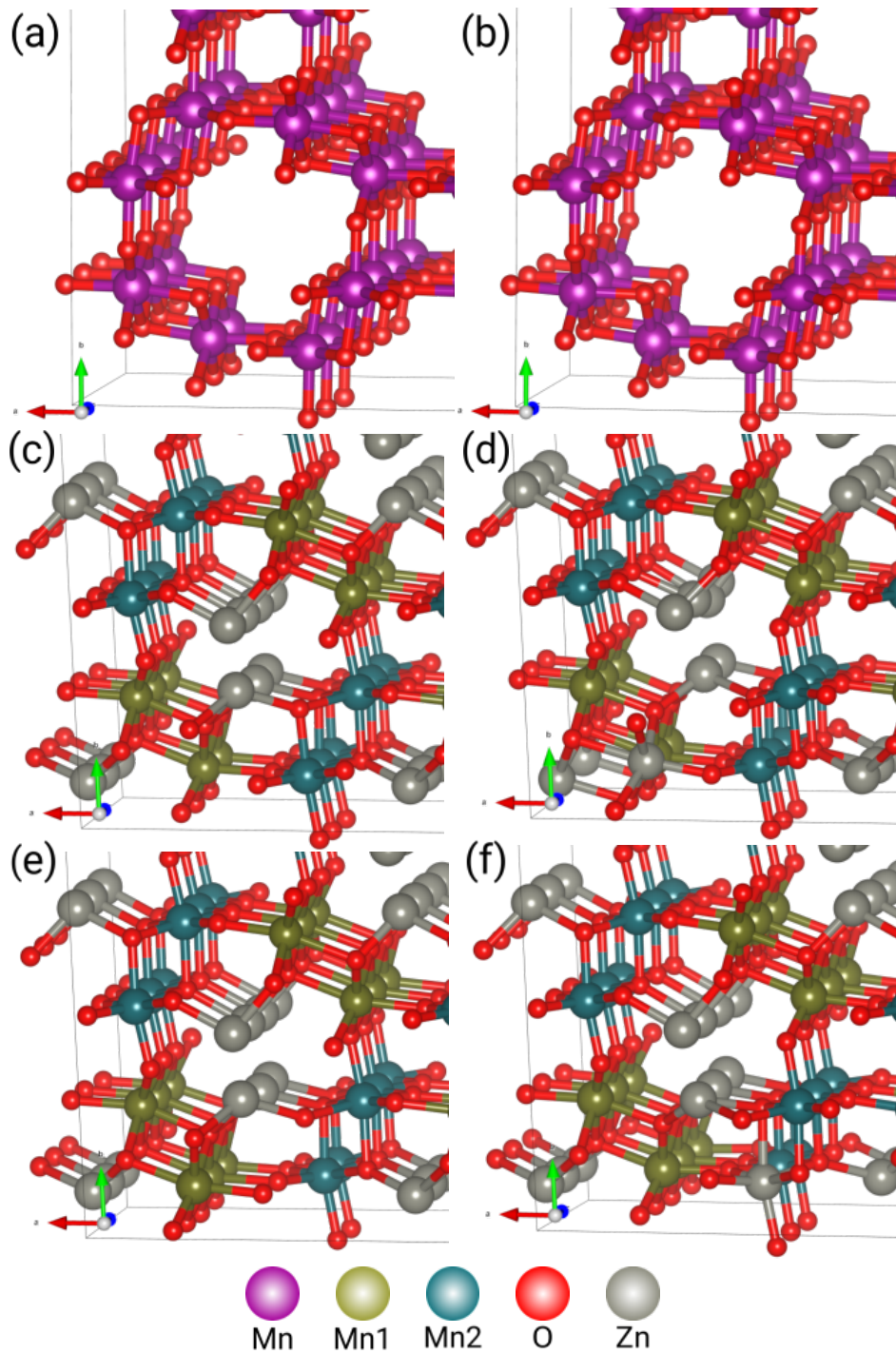


FIG. S6. Structures of (a,b) α -MnO₂(V_{Mn}), (c,d) α -ZnMn₂O₄(V_{Mn1}) and (e,f) α -ZnMn₂O₄(V_{Mn2}) before and after performing atomic relaxation.

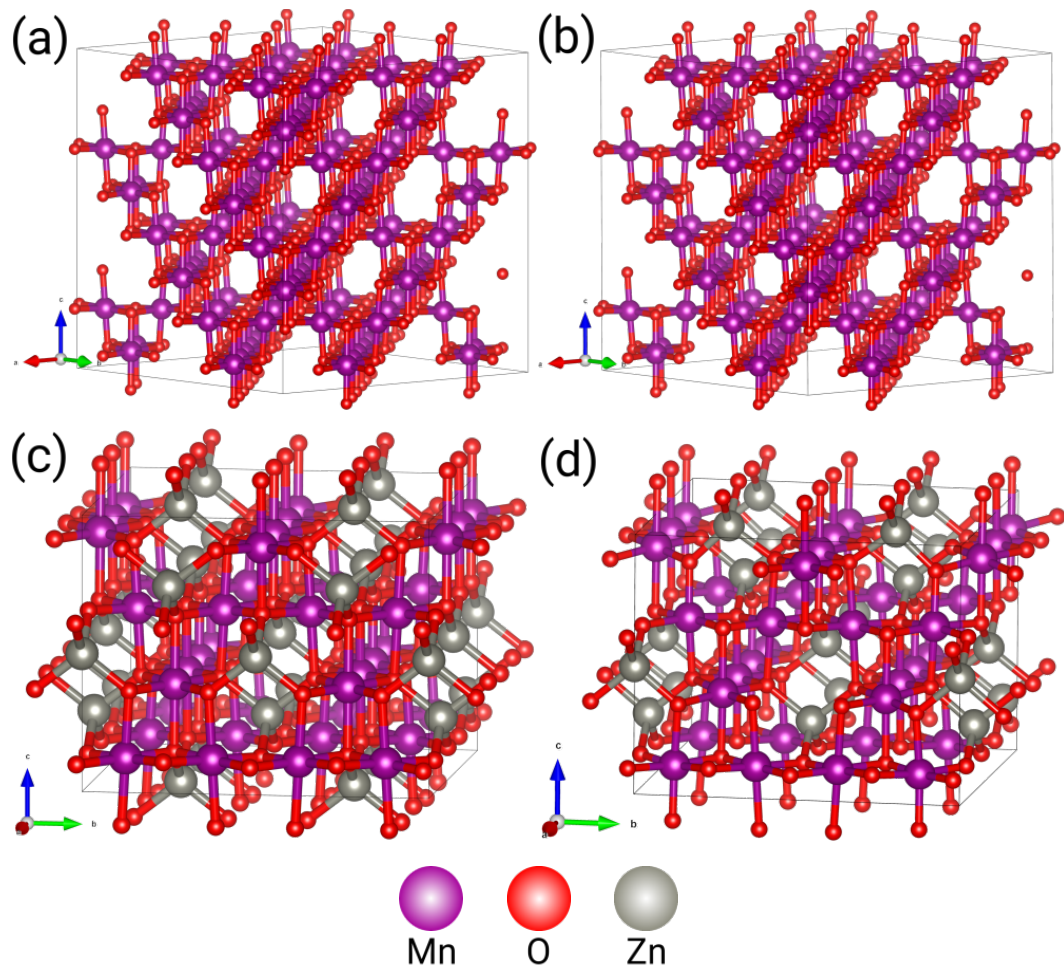


FIG. S7. Structures of (a,b) λ -MnO₂(V_{Mn}) and (c,d) λ -ZnMn₂O₄(V_{Mn}) before and after performing atomic relaxation.

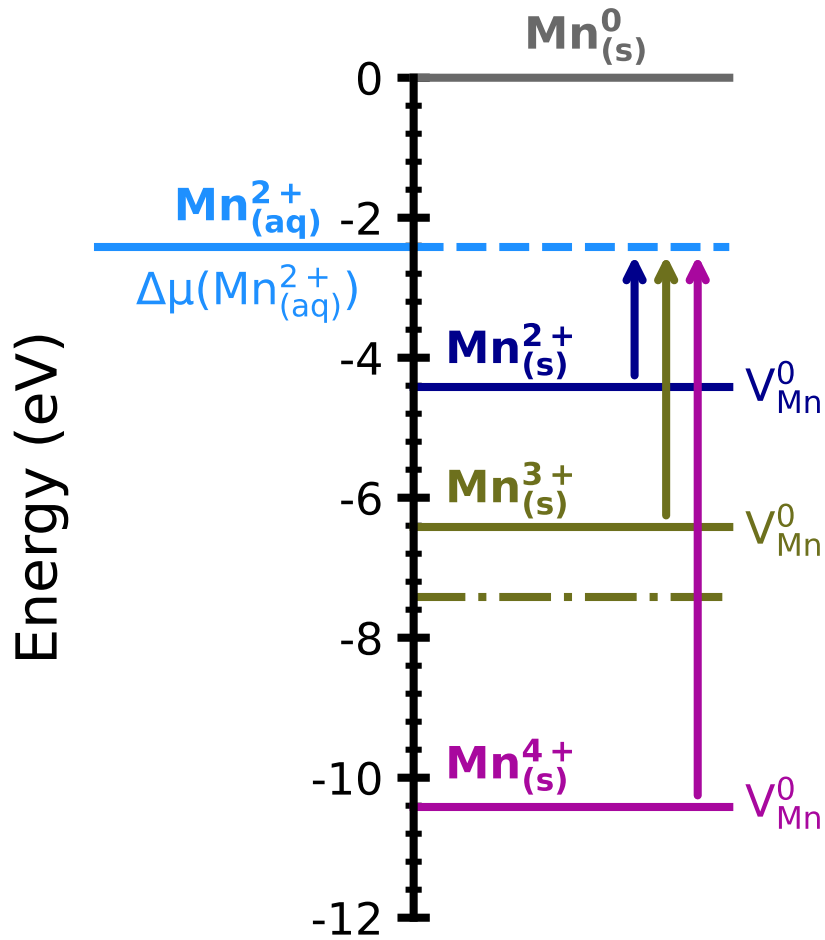


FIG. S8. Diagram relating the $E_d(V_{\text{Mn}}^0)_{\text{wor}}$ calculated for MnO ($\text{Mn}^{2+}_{(s)}$), Mn_2O_3 ($\text{Mn}^{3+}_{(s)}$) and MnO_2 ($\text{Mn}^{4+}_{(s)}$) to the chemical potential of $\text{Mn}^{2+}_{(\text{aq})}$ in the RAZIB aqueous electrolyte. The dash-dotted line indicates the $E_d(V_{\text{Mn}}^0)_{\text{wor}}$ result for ZnMn_2O_4 ($\text{Mn}^{3+}_{(s)}$).

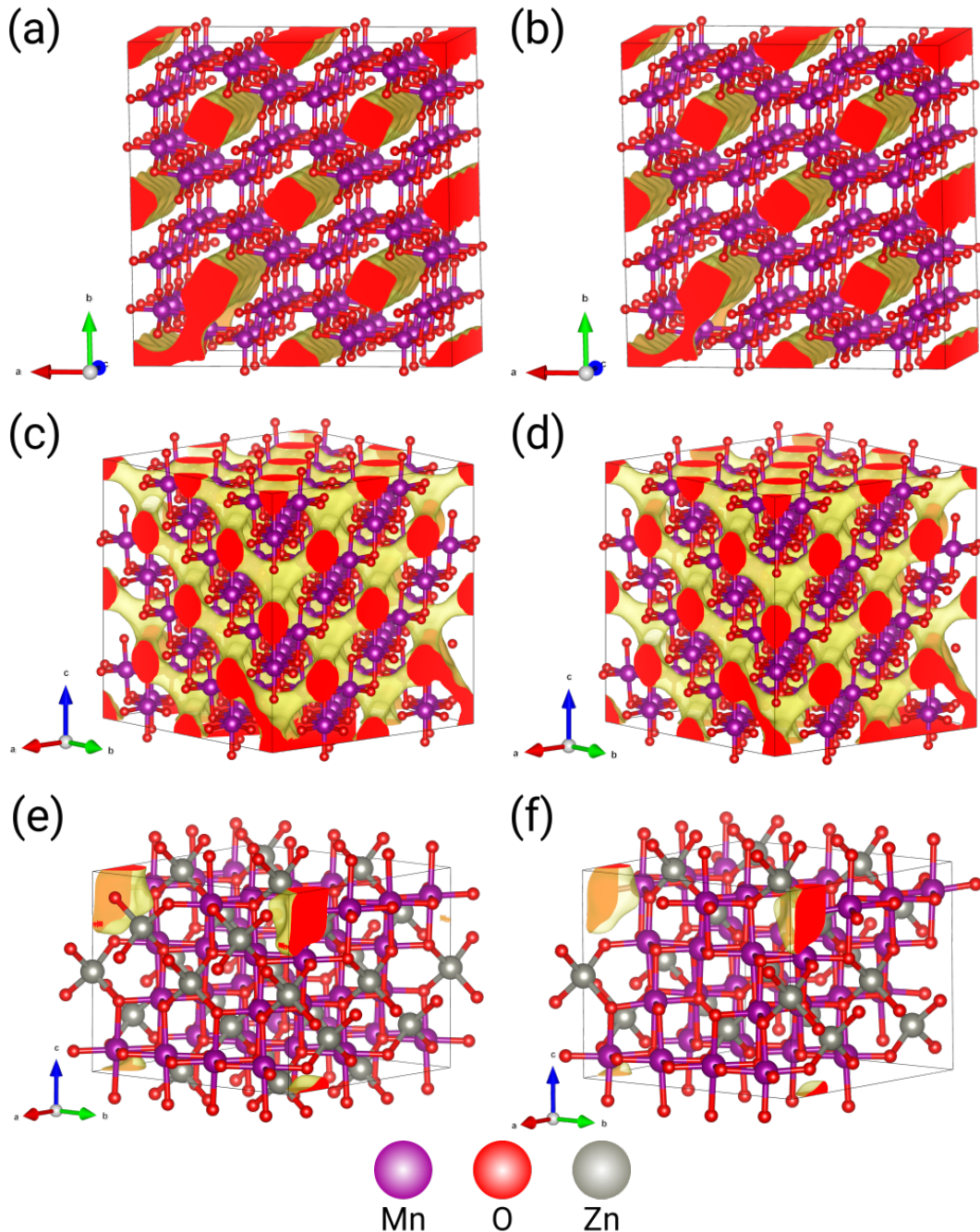


FIG. S9. Structures of (a,b) $\alpha\text{-MnO}_2(V_{\text{Mn}})$, (c,d) $\lambda\text{-MnO}_2(V_{\text{Mn}})$, and (e,f) $\lambda\text{-ZnMn}_2\text{O}_4(V_{\text{Mn}})$ before and after atomic relaxation, featuring the regions of $U_{\text{local}} > 10$ eV in each structure.

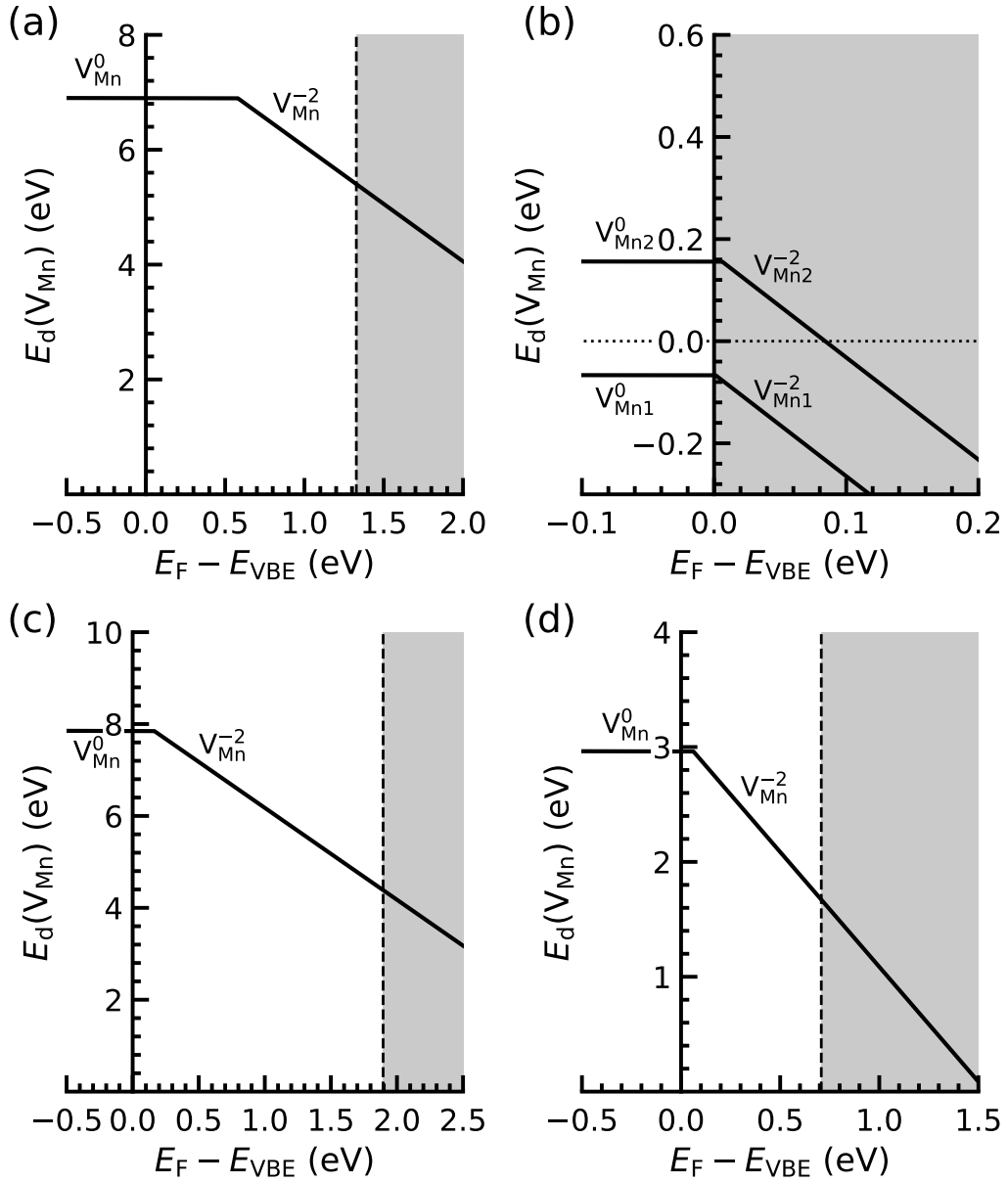


FIG. S10. Mn vacancy formation energy ($E_d(V_{\text{Mn}}^q)$) as a function of the Fermi energy (E_F) for the (a) $\alpha\text{-MnO}_2(V_{\text{Mn}})$, (b) $\alpha\text{-ZnMn}_2\text{O}_4(V_{\text{Mn}})$, (c) $\lambda\text{-MnO}_2(V_{\text{Mn}})$, and (d) $\lambda\text{-ZnMn}_2\text{O}_4(V_{\text{Mn}})$ structures. The vertical dashed lines mark the location of the conduction band edge (CBE), with the grey zones highlighting conduction band regions.